© 2020. Published by The Company of Biologists Ltd | Journal of Cell Science (2020) 133, jcs129213. doi:10.1242/jcs.129213

RESEARCH ARTICLE

Trypanosomes have divergent kinesin-2 proteins that function differentially in flagellum biosynthesis and cell viability

Robert L. Douglas, Brett M. Haltiwanger*, Anna Albisetti‡, Haiming Wu, Robert L. Jeng§, Joel Mancuso¶, W. Zacheus Cande and Matthew D. Welch**

ABSTRACT

Trypanosoma brucei, the causative agent of African sleeping sickness, has a flagellum that is crucial for motility, pathogenicity, and viability. In most eukaryotes, the intraflagellar transport (IFT) machinery drives flagellum biogenesis, and anterograde IFT requires kinesin-2 motor proteins. In this study, we investigated the function of the two *T. brucei* kinesin-2 proteins, TbKin2a and TbKin2b, in bloodstream form trypanosomes. We found that, compared to kinesin-2 proteins across other phyla, TbKin2a and TbKin2b show greater variation in neck, stalk and tail domain sequences. Both kinesins contributed additively to flagellar lengthening. Silencing TbKin2a inhibited cell proliferation, cytokinesis and motility, whereas silencing TbKin2b did not. TbKin2a was localized on the flagellum and colocalized with IFT components near the basal body, consistent with it performing a role in IFT. TbKin2a was also detected on the flagellar attachment zone, a specialized structure that connects the flagellum to the cell body. Our results indicate that kinesin-2 proteins in trypanosomes play conserved roles in flagellar biosynthesis and exhibit a specialized localization, emphasizing the evolutionary flexibility of motor protein function in an organism with a large complement of kinesins.

KEY WORDS: *Trypanosoma brucei*, Flagellum, Kinesin

INTRODUCTION

Trypanosoma brucei spp. are kinetoplastid parasites that cause African trypanosomiasis (African sleeping sickness) in humans and animals (Büscher et al., 2017; Cayla et al., 2019; Kennedy and Rodgers, 2019). They are transmitted to mammals by the tsetse fly, and progress through multiple life-cycle stages, including the insect vector procyclic form (PCF) and infective mammalian bloodstream form (BSF). In human African trypanosomiasis (HAT), the BSF proliferates extracellularly in the blood and then in the central nervous system (Kennedy and Rodgers, 2019; Krüger et al., 2018; Mogk et al., 2017). Recent progress in treating HAT, particularly the development of the oral agent fexinidazole (Mesu et al., 2018), is encouraging. Nonetheless, HAT remains a significant public health threat in sub-Saharan Africa (Kennedy, 2019). Moreover, most current treatment options have significant issues with drug resistance, toxicity, cost and difficulty of administration (Akinsolu et al., 2019; Fairlamb and Horn, 2018; Field et al., 2017). Thus, the development of new drugs remains critical.

T. brucei is highly motile, and its motility is driven by a single membrane-bound cilium (flagellum) containing a canonical 9+2 microtubule axoneme with a filamentous paraflagellar rod (PFR) (Höög et al., 2012; Langousis and Hill, 2014; Ralston et al., 2009). The flagellum attaches to the cell body along the flagellar attachment zone (FAZ), a specialized structure running beneath the cytoplasmic face of the plasma membrane along most of the length of the flagellum (Langousis and Hill, 2014; Sunter and Gull, 2016; Taylor and Godfrey, 1969). The FAZ contains four specialized subpellicular microtubules (the microtubule quartet, MtQ, which initiates at the basal body and continues to the anterior cell tip), associated intracellular membranes contiguous with the endoplasmic reticulum (ER) and nuclear envelope (NE), and a filament system that connects to the axoneme and PFR via several membrane-spanning structures (Höög et al., 2012; Kohl and Bastin, 2005; Ralston et al., 2009; Sunter and Gull, 2016; Zhou et al., 2015). The flagellum beats in distinctive wave patterns that are adapted for movement in the bloodstream of mammalian hosts (Heddergott et al., 2012; Krüger et al., 2018; Rodríguez et al., 2009). Movement of BSF *T. brucei* is essential for cell viability and cytokinesis (Broadhead et al., 2006; Ralston and Hill, 2006), virulence (Shimogawa et al., 2018), development and pathogenesis (Langousis and Hill, 2014), and evasion of complement-mediated cell killing (Engstler et al., 2007; Heddergott et al., 2012).

The biogenesis of flagella requires the intraflagellar transport (IFT) machinery, which consists of an evolutionarily conserved suite of IFT proteins (Taschner and Lorentzen, 2016; van Dam et al., 2013), and kinesin and dynein motors (Prevo et al., 2017; Scholey, 2013). This machinery is under dynamic regulation to control flagellar structure and function (Ishikawa and Marshall, 2011). The IFT machinery moves cargoes along the axoneme in IFT trains (Cole et al., 1993, 1998; Kozminski et al., 1993; Lechtreck, 2015; Pigino et al., 2009), and mediates cargo entry into and exit from the flagellar compartment (Buisson et al., 2013; Dishinger et al., 2010; Kee et al., 2012; Verhey et al., 2011). Anterograde IFT transport is driven primarily by kinesin-2 family motor proteins (Prevo et al., 2017; Scholey, 2013), including two major subfamilies: heterotrimeric kinesin-2, comprising two different kinesin motor subunits (2A and 2B; KRP85 and KRP95, or KIF3A and KIF3B in vertebrates) (Cole et al., 1993; Kozminski et al., 1995) and the non-motor kinesin-associated protein (KAP, or KAP3A/3B in vertebrates) (Mueller et al., 2005; Wedaman et al., 1996); and in metazoans, homodimeric kinesin-2, which consists of two identical (2C; OSM3, or KIF17 in vertebrates) motor subunits (Prevo et al., 2017; Scholey, 2013; Signor et al., 1999). In metazoans, these two subfamilies have been shown to act both cooperatively and independently in IFT (Insinna and Besharse, 2008; Prevo et al., 2015; Snow et al., 2004). Kinesin-2 proteins also

Department of Molecular & Cell Biology, University of California, Berkeley, CA 94720, USA.
*Present address: University of Texas, Health Science Center, Houston, TX 77030, USA. ‡Present address: Swiss Tropical and Public Health Institute, Basel, Switzerland. §Present address: Intercept Pharmaceuticals, San Diego, CA 92121, USA. ¶Present address: Carl Zeiss Microscopy, Thornwood, NY 10594, USA.

**Author for correspondence (welch@berkeley.edu)

A.A., 0000-0001-7800-443X; M.D.W., 0000-0003-2537-6349

Handling Editor: Michael Way
Received 28 March 2013; Accepted 27 May 2020

Journal of Cell Science (2020) 133, jcs129213. doi:10.1242/jcs.129213

participate in extraciliary processes including transport of organelles, proteins, RNAs and virus cargoes, mitosis, cytokinesis, cell polarization, and cell adhesion and development (Prevo et al., 2017; Scholey, 2013).

In this study, we investigate the function of kinesin-2 proteins in BSF *T. brucei*. The *T. brucei* genome encodes ∼48 kinesins, including two kinesin-2 proteins (Berriman et al., 2005; Bertiaux et al., 2018a; Wickstead et al., 2010a), TbKin2a and TbKin2b. Our bioinformatic analysis suggests that TbKin2a and TbKin2b lack common sequence motifs that are broadly conserved in kinesin-2 proteins, and *T. brucei* lacks a gene encoding a homolog of the KAP subunit, which is required for heterotrimer function. We further found that both TbKin2a and TbKin2b contribute to flagellar biosynthesis in BSF *T. brucei*. Interestingly, silencing TbKin2a inhibits cell proliferation, cytokinesis and motility, whereas silencing TbKin2b does not. Moreover, TbKin2a localizes to the FAZ, suggesting it functions both within the flagellum and cell body. Thus, kinesin-2 proteins in trypanosomes play both canonical and unanticipated roles.

RESULTS

T. brucei has two divergent kinesin-2 proteins

The *T. brucei brucei* genome encodes the kinesin-2 proteins TbKin2a (Tb927.5.2090) and TbKin2b (Tb927.11.13920) (Fig. 1A), which were classified according to their motor domain (MD) sequences (Berriman et al., 2005; Wickstead and Gull, 2006; Wickstead et al., 2010a) using phylogenetic inference analysis (Goodson et al., 1994; Wickstead et al., 2010a) (see Fig. S1A for kinesin-2 phylogenetic tree from Wickstead et al., 2010a; see Table S1 for MD sequence identity comparisons). However, sequences in the kinesin-2 the neck-stalk-tail (NST) region, while not as well conserved as MD sequences (average of 17% NST sequence identity versus 54% MD sequence identity), are also important for kinesin function in metazoan species (De Marco et al., 2001; De Marco et al., 2003; Doodhi et al., 2009; Imanishi et al., 2006; Vukajlovic et al., 2011) (see Table S2 for identity comparison of NST sequences). Nevertheless, systematic analysis of kinesin-2 NST sequence motifs in a broad evolutionary context has been limited. We thus sought to further categorize kinesin-2 proteins based on NST sequences.

We compiled a phylogenetically diverse set of 81 kinesin-2 sequences from 25 species (Table S3A), which represent a broad cross-section of known phylogenetic diversity, and used the multiple Em for motif elicitation (MEME) tool suite to analyze these sequences (Fig. 1B–D; Figs S1 and S2, Table S3A,B). MEME identified a single amino acid motif consistent with a kinesin-2 neck domain at the beginning of the NST domain for all kinesin-2 proteins in our data set (Case et al., 2000; Vale and Fletterick, 1997). MEME also identified over 20 additional, statistically significant NST sequence motifs that can be sorted into distinct ordered motif groups and are broadly conserved across all kinesin-2-containing eukaryotic superfamilies from Metazoa to Excavata (Fig. 1D). Notably, motifs forming a primary (1°) motif group were common to almost all protist and metazoan taxa. A secondary (2°) motif group frequently associated with coiled-coil domains, as well as motifs that are specific to subgroups 2A and/or 2B, were also widely shared among protists and metazoa (Fig. 1B–D; Figs S1B,C; S2). The assignment of protist taxa encoding kinesin-2 into subgroups 2A and 2B was not observed in the phylogenetic analyses using MD sequences. MEME also assigned 2C motifs to metazoan kinesin-2C taxa, but such motifs were absent from protist taxa. The primary exception was a single 2C motif shared among kinetoplastids and metazoans, as discussed below (Fig. 1B–D; Figs S1 and S2).

The greatest divergence in NST sequence motifs occurs within the kinetoplastids, including *T. brucei* (Fig. 1B–D). Kinetoplastid kinesin-2 NST domains are longer, have more extensive predicted coiled-coil sequences, and lack most motif groups that are present in other protists and metazoans (Fig. 1; Fig. S2). Instead, the kinetoplastids have unique motif groups (knto/k) that are specific to these organisms. Parasititic kinetoplastid species (Julkowska and Bastin, 2009) and the free-living kinetoplastid *Bodo saltans*, lack the KAP subunit (k3) (Fig. 1B,D), which is required for kinesin-2 heterotrimer function and is present in all other organisms included in our analysis. Surprisingly, MEME assigned, to the kinetoplastid homologs of TbKin2b, a single, statistically significant kinesin-2C (OSM3) motif that is also present only in metazoan taxa (Fig. 1B–D,E; Figs S1 and S2). Together, these results suggest that kinetoplastid kinesin-2 proteins do not have a heterotrimeric structure consisting of a canonical 2A, 2B and KAP subunits, and raise the possibility that kinesin-2 proteins from kinetoplastid species may form homodimers and/or heterodimers. Thus, MEME analysis of NST sequences suggests that kinesin-2 proteins in *T. brucei* have diverged from such proteins in other organisms, raising questions about the extent to which their canonical functions are conserved in trypanosomes and whether novel functions have evolved.

TbKin2a distributes along the length of the flagellum, with stronger localization near the basal body

To assess the function of kinesin-2 proteins in *T. brucei*, we raised antibodies to a portion of the stalk domain. These specifically recognize the ∼130 kDa TbKin2a protein on immunoblots of whole-cell lysates (Fig. S3). We next assessed TbKin2a localization in BSF cells by immunofluorescence microscopy. TbKin2a localized in a punctate pattern along the lengths of both old and new flagella (Fig. 2A). During the cell cycle, TbKin2a staining intensity on flagella increased, and the relative staining between old and new flagella remained roughly equivalent, except that TbKin2a typically showed significantly enhanced staining on new flagella relative to old flagella during the one dividing kinetoplast, one nucleus (1K*1N) stage, when there is new flagellum growth. This reflects cytoskeletal remodeling at the posterior end associated with the emergence of the new flagellum (Gluenz et al., 2011; Ikeda and de Graffenried, 2012; Lacomble et al., 2010; Wheeler et al., 2013). We also determined the mean fluorescence intensity along full-length flagella. Using the peak intensity of DAPI-stained kinetoplast DNA as a posterior reference point (Fig. 2B), we determined that the flagellar intensity profile (on both old and new flagella) had two peaks at ∼0.7 µm and ∼2.1 µm, approximating locations near the basal body and flagellar pocket collar. Past the second peak, staining diminished to the anterior tip, where it increased slightly, with 65% of integrated staining intensity being confined to the proximal half of the flagellum.

TbKin2a also localized in the region of the kinetoplasts and basal bodies throughout their duplication cycle (Fig. 2C–F). There was extensive overlap between TbKin2a and the proximal end of basal bodies, as marked by the basal body marker BBA4 (Hoffmann et al., 2018; Schneider and Ochsenreiter, 2018; Woods et al., 1989) (Fig. 2G,H). TbKin2a and BBA4 colocalized with kinetoplastid DNA near the proximal ends of basal bodies (Fig. 2G,H). Thus, TbKin2a is positioned on the basal body adjacent to the kinetoplast.

TbKin2a colocalizes with IFT proteins primarily at the flagellum base

Although the canonical role of kinesin-2 proteins is in IFT (Lechtreck, 2015; Scholey, 2013), the divergent sequences of

Journal of Cell Science (2020) 133, jcs129213. doi:10.1242/jcs.129213

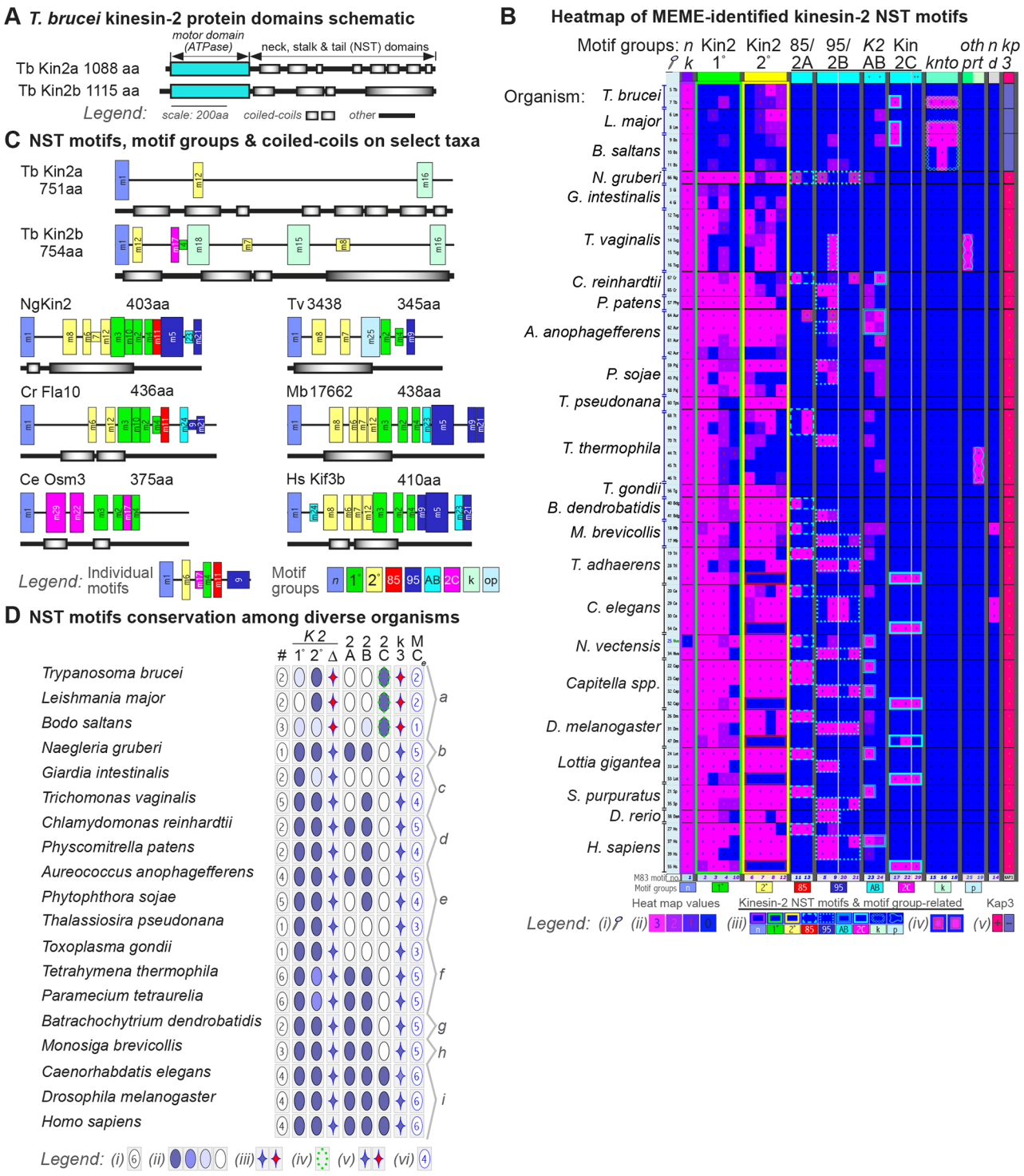

Fig. 1. See next page for legend.

TbKin2a and TbKin2b raised the question of whether they retain their function in IFT in trypanosomes. In *T. brucei*, a full complement of canonical IFT complex B (anterograde; IFTB) and IFT complex A (retrograde; IFTA) and Bardet–Biedl syndrome (BBSome) proteins have been identified and shown to localize to the flagellum and basal body regions (Absalon et al., 2008; Adhiambo et al., 2009; Franklin and Ullu, 2010; van Dam et al., 2013). They have also been shown to interact and function in IFT (Bertiaux et al., 2018b; Bhogaraju et al., 2013; Blisnick et al., 2014; Buisson et al., 2013; Fort et al., 2016; Huet et al., 2014, 2019; Wachter et al., 2019). We co-stained for TbKin2a with IFTB marker IFT172 (Fig. 3A–D) or IFTA marker IFT144 (Fig. 3E). As previously reported in PCF cells (Absalon et al., 2008), in BSF cells these markers exhibited punctate staining along the flagellum and increased intensity near basal bodies. Along the flagellum, there was little colocalization between TbKin2a and either IFT172 or IFT144 (Fig. 3A,C,E,F; mean Mander's colocalization coefficients 0.164 and 0.278, respectively). However, we did observe clear patterns of

Journal of Cell Science

Journal of Cell Science (2020) 133, jcs129213. doi:10.1242/jcs.129213

Fig. 1. MEME analysis of kinesin-2 sequences from diverse species. (A) Schematic of TbKin2a and TbKin2b domains. (B) Heatmap showing results from one representative MEME run (MEME 83). See Figs S1, S2, and Table S3 for detailed MEME results. Rows represent 68 taxa [legend (at bottom): (i) species abbreviations require magnification and are explained in Table S3B]. Columns represent 26 statistically significant motifs clustered into groups (based on total E-values; also see Fig. S1B; motif 29 was not statistically significant). Each taxon and motif is color-coded based on motif *P*-values [legend (ii): from heat map value (hmv) of 3 (magenta) to 0 (blue), indicating taxon-specific individual motif *P*-values as: 3=*P*-value $\leq 1\times10^{-10}$, 2=*P*-value $>1\times10^{-10}$ and $\leq 1\times10^{-08}$, 1=*P*-value $>1\times10^{-08}$ and $\leq 1\times10^{-05}$, and 0=*P*-value $>1\times10^{-05}$]. Motif groups are also color-coded [legend (iii): neck (nk or n), motif 1; 1° kinesin-2 (Kin2 1° or 1°), motifs 2, 3, 4, 10; 2° kinesin-2 (Kin2 2° or 2°), motifs 6, 7, 8, 12; KRP85-specific motifs (Kin2A or 2A), motifs 11, 13; KRP95-specific motifs (Kin2B or 2B), motifs 5, 9, 20, 21; present in both KRP85/Kin2A and KRP95/Kin2B (K2AB or AB), motifs 23, 24; Osm3-specific homodimeric (Kin2C or 2C), motifs 17, 22, 29; kinetoplastid-specific (knto or k), motifs 15, 16, 18; other protist-specific (op or p), motifs 19, 25; undefined (nd), motif 14]. In rare cases, a single taxon had both 2A and 2B motifs [legend (iv)]. The far-right column indicates presence/absence of the KAP3 subunit in each taxon [legend (v): with KAP 3+, red square; no KAP3–, blue square]. (C) NST motif and coiled-coil domain schematics for TbKin2a, TbKin2b, and other representative kinesin-2 proteins. Motif sequences are in Fig. S1. A key to labels and colors is in Fig. S2A. Motif widths are scaled to sequence length, and motif heights indicate *P*-value ranges (see Fig. S2B). See Fig. S2D–F for schematics of representative kinesin-2 proteins. (D) NST motif and motif group distribution among a phylogenetically diverse sampling of eukaryotes with kinesin-2 proteins. Rows represent species. Column designations are as follows: (#) the number of kinesin-2 proteins in the species [legend (at bottom) (i): number of taxa]; (1°, 2°) the frequency that 1° and 2° motifs occur by color coding [legend (ii): dark blue≥2 motifs at a hmv=3, medium blue ∼1 motif at hmv=3 or ∼2 motifs at hmv=2, light blue ∼1 motif at hmv=2 or >2 motifs at hmv=1, unfilled values<previous categories]; (Δ) whether the order and location of motifs is typical (blue) or atypical (red) [legend (iii): blue star typical, red star atypical]. For additional information, see Fig. S2C. (2A, 2B) indicates the frequency that 2A and 2B motifs occur by color coding [legend (ii): dark blue ≥1 motif at hmv=3, medium blue≥∼1 motif at hmv=2, light blue≥∼1 motifs at hmv=1]; (2C) the presence of a 2C motif assignment [legend (iv): motif assignments to kinetoplastids are outlined with green dots]; (k3) the presence (blue) or absence (red) of genes encoding KAP3 homologs [legend (v): blue star Kap3 present, red star Kap3 absent]; (MC) the number of kinesin-2 NST motif groups conserved within that species, out of 6 primary motif groups [legend (vi): number of motif groups]. The letters a–i to the right show phylogenetic groups: (a) kinetoplastids, (b) heterobolosea (both Discoba), (c) Metamonada, (d) algae and plants with flagellated cells (Archaeplastida), (e) stramenopiles (superphylum Stramenopile-Alveolata-Rhizaria, SAR), (f) alveolata (including apicomplexia) (SAR), (g) fungi (Nucletmycea), (h) choanoflagellates (i) metazoa (both Holozoa). See Adl et al. (2019).

colocalization of TbKin2a and IFT172 (Fig. 3A–D,F) and TbKin2A and IFT144 (Fig. 3E,F) in the region near the kinetoplasts and basal bodies, near the proximal ends of flagella (Fig. 3E,F; mean Mander's colocalization coefficients for TbKin2a–IFT172 and TbKin2a–IFT144 of 0.655 and 0.636, respectively). This suggests that TbKin2a might interact indirectly with IFT complex proteins primarily near the flagellum base.

TbKin2a localizes to the FAZ throughout the cell cycle

Given the tight association of the flagellum with the FAZ, we sought to distinguish whether TbKin2a also localizes to the FAZ. The flagellum can be detached from the cell-body side of the FAZ and cell body by detergent extraction, which permits separate visualization of the components localized to each structure (Robinson et al., 1991). Surprisingly, at all stages of the cell cycle, endogenous TbKin2a colocalized with the intracellular FAZ marker L3B2 (Kohl et al., 1999) in a continuous punctate pattern from the initiation of the FAZ (start of L3B2 staining) near the flagellar pocket collar (Lacomble et al., 2009, 2010) to the cell anterior tip (Fig. 4A). (We did not observe IFT172 colocalization with the FAZ, data not shown.)

Because detergent extraction significantly diminished TbKin2a staining on flagella (as also observed with IFT proteins; Absalon et al., 2008), we sought to identify conditions to separate the flagellum and FAZ following fixation and without detergent extraction. We observed that the flagellum and FAZ were sometimes partially separated due to shear forces during mounting. Under these circumstances, TbKin2a could always be seen on both structures (Fig. 4B,C). We could also use deliberate controlled shearing to induce similar separation of the flagellum and FAZ post-fixation, and under these circumstances, TbKin2a could similarly be seen on both structures (Fig. 4D). To further confirm these results, we triggered flagellar detachment in living cells through Ca^{2+} chelation (Vickerman, 1969), either by treatment with citrate or EGTA. This treatment resulted in cells with detached flagella, including 1K1N cells with a full-length FAZ and one flagellum that is mostly detached from the cell body, except at the flagellar base. In these cells, TbKin2a was localized to both the flagellum and FAZ (Fig. 4E; Fig. S4).

Finally, to rule out the possibility that the anti-TbKin2a antibody non-specifically recognizes FAZ components, we engineered BSF cells to express C-terminally Myc-tagged TbKin2a (TbKin2a–Myc) (Fig. S5A) and stained these cells with anti-Myc antibody. TbKin2a–Myc also colocalized with the FAZ marker L3B2 (Fig. S5B). TbKin2a staining continued to the basal body area, separate from its staining on flagella, proximal to the FAZ initiation point. Collectively, these results indicate that TbKin2a associates with the FAZ as well as with the flagellum, most likely on the MtQ, which is the sole intracellular cytoskeletal element know to connect from the basal body to the FAZ.

Silencing of TbKin2a inhibits proliferation of BSF *T. brucei*, whereas silencing of TbKin2b does not

To determine the importance of kinesin-2 proteins in BSF *T. brucei*, we used RNA interference (RNAi) to silence expression of TbKin2a, TbKin2b or both. TbKin2a mRNA was diminished at 24 h and 48 h post induction (hpi) of dsRNA expression in TbKin2a-silenced cells, but remained unaffected in TbKin2b-silenced cells, as assessed by RT-PCR (Fig. 5A) and quantitative (q)RT-PCR (Fig. 5B). Similarly, TbKin2b mRNA was diminished at 24 hpi and 48 hpi in TbKin2b-silenced cells, but was unaffected in TbKin2a-silenced cells (Fig. 5A,B). Both mRNAs were diminished in TbKin2a2b-silenced cells. For TbKin2a, protein expression remained at 24 hpi but was strongly diminished after 48 hpi (Fig. 5A; Fig. S3B).

Interestingly, TbKin2a-silenced cells proliferated 50–70% more slowly than uninduced cells after 24 hpi and ceased proliferation by 48 hpi (Fig. 5C). For TbKin2b-silenced cells, proliferation did not decrease significantly by 72–96 hpi (Fig. 5C). Silencing both TbKin2a and TbKin2b together resulted in a cessation of proliferation with kinetics similar to single TbKin2a knockdown (Fig. 5C). Thus, cell proliferation in BSF *T. brucei* requires TbKin2a, but proliferation is not affected by RNAi silencing of TbKin2b.

Evidence of the essential role of TbKin2a in cell proliferation led us to assess its role in cell cycle progression. We first counted the numbers and observed the morphology of nuclei and kinetoplasts at various time points after RNAi induction (Fig. 5D). Beginning at 24 hpi, the proportion of normal 1K1N (1 kinetoplast, 1 nucleus), 2K1N, and 2K2N cells decreased progressively, while abnormal

Journal of Cell Science (2020) 133, jcs129213. doi:10.1242/jcs.129213

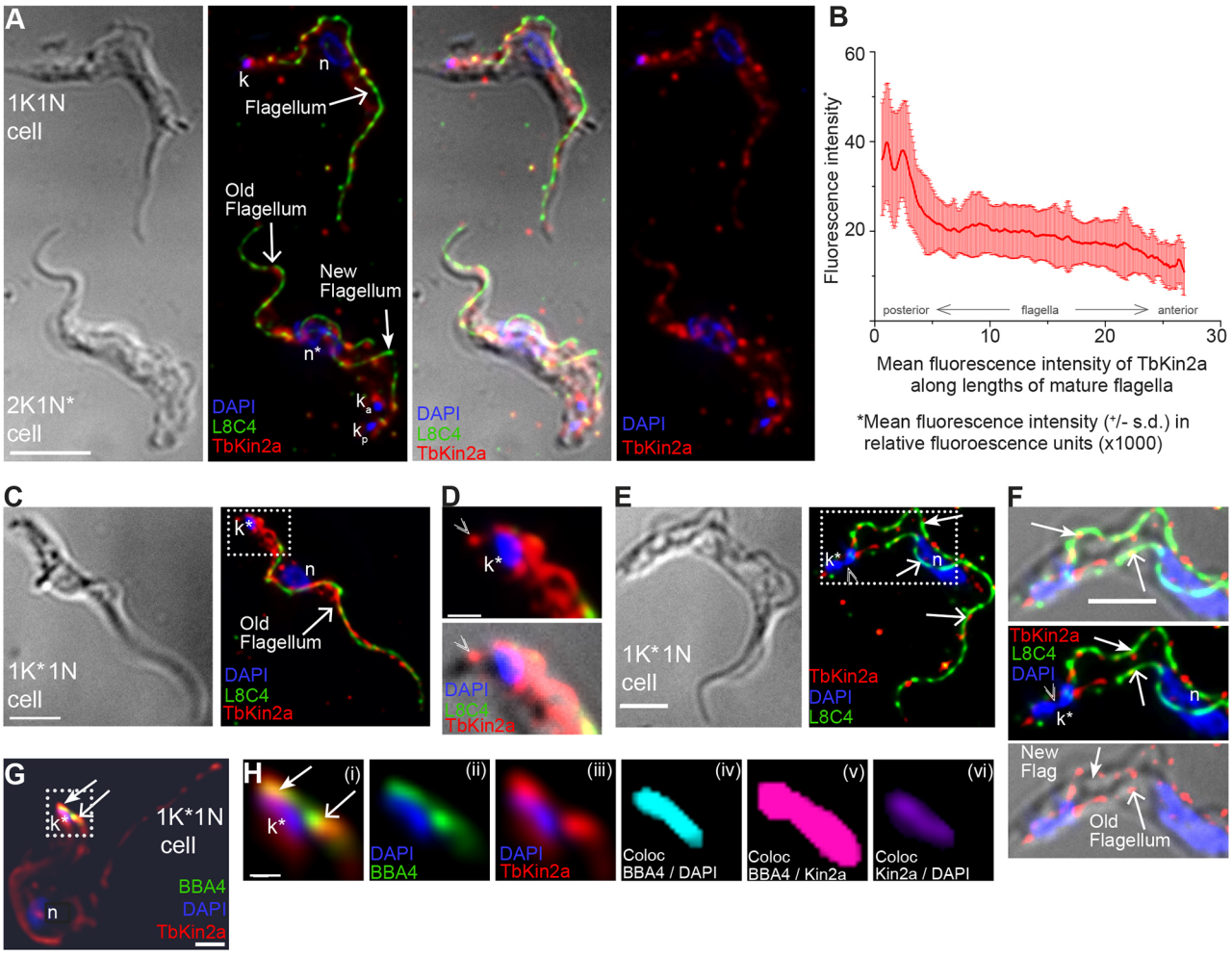

Fig. 2. TbKin2a localizes to flagella and basal bodies. (A) Differential interference contrast (DIC) and immunofluorescence images of BSF (90-13) cells stained for TbKin2a (red), paraflagellar rod protein (PFR) as a flagellar marker (green, L8C4) and DNA (blue, DAPI). (B) TbKin2a mean relative fluorescence intensity along full-length BSF flagella (measured every 0.1 µm from basal body to flagellum anterior end). Mean flagellum length=23 µm. Error bars, s.d. (*n*=50). (C) 1K*1N cell stained for the PFR (green, L8C4), TbKin2a (red), and DNA (blue, DAPI). (D) Magnification of area boxed in C. Double V indicates TbKin2a staining posterior to dividing kinetoplast. (E) DIC and immunofluorescence images of a 1K*1N cell stained for the PFR (green, L8C4), TbK2a (red) and DNA (blue, DAPI). (F) Magnification of area boxed in E. Doubled V indicates narrow connection between two parts of a nearly fully divided kinetoplast (Gluenz et al., 2011). (G) Immunofluorescence image of a 1K*1N cell stained for basal bodies (green, BBA4), TbKin2a (red) and kinetoplast DNA (blue, DAPI). (H) Magnification of area boxed in G showing: (i–iii) a region near dividing kinetoplast and basal bodies; and, (iv–vi) 2D projections of single-color volume renderings showing colocalization and extent of 3D voxels having greater-than-threshold adjusted signal colocalization between BBA4 and DAPI (cyan), BBA4 and TbKin2a (pink), and TbKin2a and DAPI (purple). (A, C–H) Immunofluorescence images corresponding to two-dimensional (2D) maximum intensity projections from a three-dimensional (3D) deconvolved *z*-stacks. Abbreviations and symbols: wide arrow, flagellum (interphase) or old flagellum; narrow arrow with filled arrowhead, new flagellum; k, kinetoplast; k*, dividing kinetoplast; k_a, anterior kinetoplast; k_p, posterior kinetoplast; n, nucleus; n*, mitotic nucleus. Scale bars: 5 µm (A); 3 µm (C–F); 2.4 µm (G); 0.75 µm (H).

cells with multiple nuclei and kinetoplasts (xK†yN†) or with one abnormally large nucleus and multiple kinetoplasts (xK†1N†), increased progressively (Fig. 5D). We next observed the effect of TbKin2a silencing on the cell cycle state by FACS (Fig. 5E). From 24 hpi to 48 hpi, the percentage of cells with 2C DNA content decreased, whereas the percentage of cells with 4C DNA content increased. After 48 hpi, there was a significant increase in the proportion of cells with ≥4C DNA content. This suggests that nuclear DNA synthesis continued without complete nuclear separation and/or cytokinesis.

At the morphological level, cells induced for 24 h or longer became much larger than uninduced cells, accumulating multiple nuclei, flagella (Fig. 5F,G) and FAZ (Fig. 5H). Typically, flagella and FAZ clustered at the anterior ends of undivided cells, and there was little evidence of cleavage furrow formation or progression (Fig. 5F,G,H). These results suggest that TbKin2a is important for cytokinesis, which initiates at the anterior end (Sherwin and Gull, 1989).

In addition, at 24 hpi, 48 hpi and 72 hpi, TbKin2a and TbKin2a2b-silenced cells showed nuclei that were often poorly defined or separated, resulting in large undivided or partially divided nuclear masses with numerous nucleoli (Fig. 5G–I). Although kinetoplast DNA replication appeared to continue, ∼8–10% of kinetoplasts appeared to be partially separated or not separated (Fig. 5G–I). Basal body duplication and separation were also ongoing, but we observed multiple TbKin2a- and TbKin2a2b-silenced cells with basal bodies having no associated kinetoplast DNA (Fig. 5J). These results suggest that TbKin2a contributes to separation of nuclei and kinetoplasts, and might play a role in the association of basal bodies with kinetoplasts.

Journal of Cell Science (2020) 133, jcs129213. doi:10.1242/jcs.129213

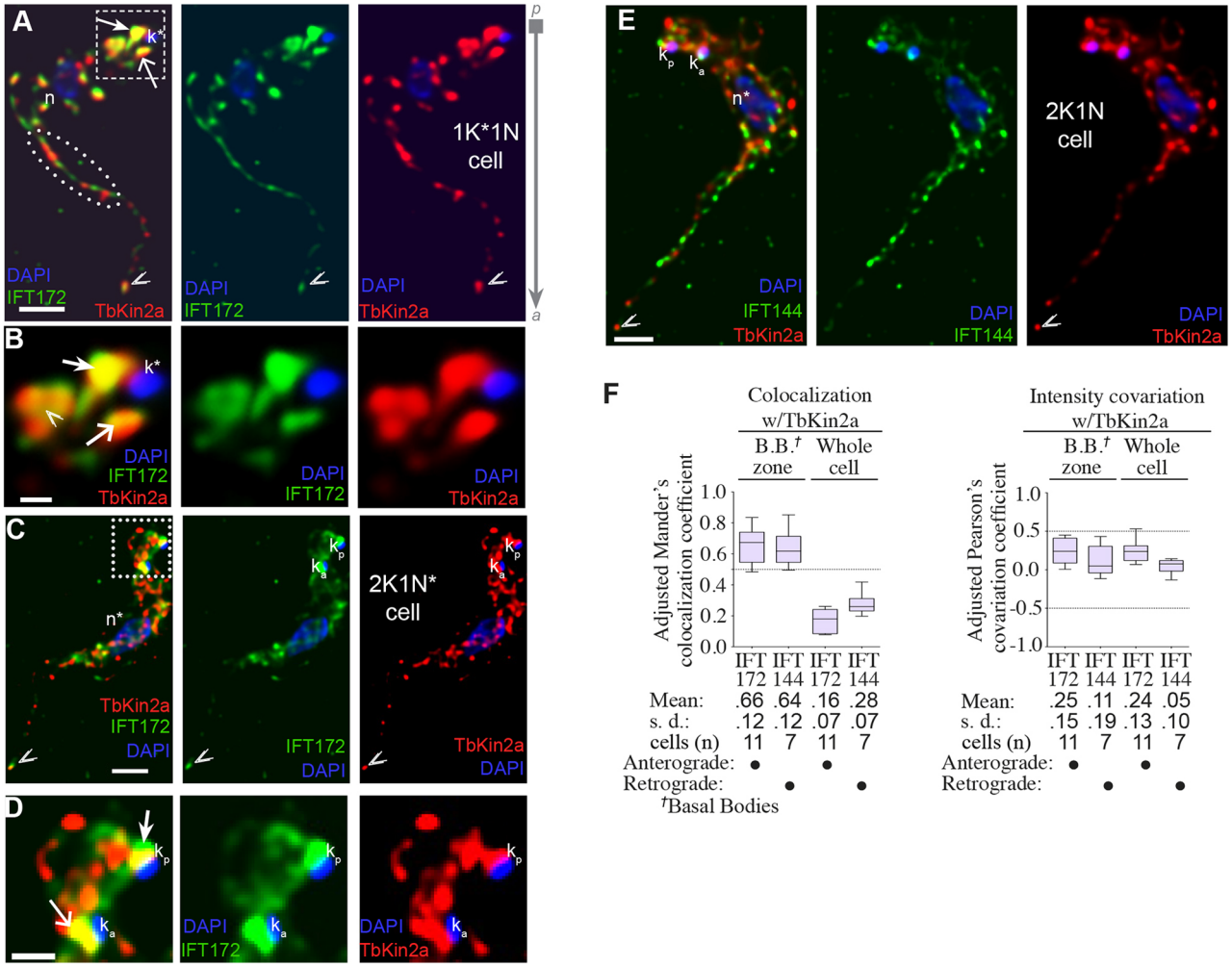

Fig. 3. Colocalization of TbKin2a with IFTA and IFTB proteins. (A) Immunofluorescence images of 1K*1N cell stained for IFT172 (green), TbKin2a (red), and DNA (blue, DAPI). Voxels with colocalized IFT172 and TbKin2a are gold. Dotted-ellipse shows area in anterior half of flagellum having alternating localization of IFT172 and TbKin2a. (B) Magnification of boxed area in A showing the region near basal bodies. See also comment in D. (C) 2K1N* cell stained as in A. (D) Higher magnification view of boxed area in C showing the region near basal bodies. Comparison of staining near basal bodies from B and D shows typically increased TbKin2a and IFT172 staining at and near base of new flagellum (double-V symbol) for 1K*1N stage cells in B relative to 2K1N* cells in D. (E) 2K1N cell stained for IFT144 (green), TbKin2a (red) and DNA (blue, DAPI). (A–E) Immunofluorescence images are presented as 2D maximum intensity projections from 3D deconvolved *z*-stacks. Abbreviations and symbols are the same as Fig. 2. (F) Threshold-adjusted Mander's colocalization coefficient and Pearson's covariation coefficient graph and statistics calculated for (i) the region immediately surrounding basal bodies, and (ii) the whole cell, to show colocalization of TbKin2a with IFT172 or IFT144 (for TbKin2a/ IFT172, *n*=11; for TbKin2a/IFT144, *n*=7). The box represents the 25–75th percentiles, and the median is indicated. The whiskers show high and low values. Scale bars: 2 µm (A,E); 0.7 µm (B); 2.5 µm (C); 1 µm (D).

TbKin2a and TbKin2b act additively in forming full-length flagella, but only TbKin2a is required for motility

Considering the established role of kinesin-2 in flagellar assembly in other organisms, we evaluated the effect of silencing TbKin2a and/or TbKin2b on flagella length. Surprisingly, given their sequence divergence from other kinesin-2 proteins, silencing either TbKin2a or TbKin2b for 72 h caused a decrease in flagellum length of 22% and 21%, respectively (Fig. 6A). Silencing both together caused an approximately additive 42% decrease in flagellar length. We could not observe whether a subpopulation of flagella remained long, in contrast with recent observations for silencing IFT proteins in PCF *T. brucei* (Bertiaux et al., 2018a; Fort et al., 2016), as the cytokinesis defect and buildup of polyploid cells caused by TbKin2a or TbKin2a2b silencing precludes separate identification of old and new flagella. This indicates that TbKin2a and TbKin2b act additively to build and/or maintain the flagellum in BSF *T. brucei*.

To determine whether the defects in flagellar length and IFT protein localization caused by TbKin2a silencing were linked with gross ultrastructural defects in the flagellum, we examined TbKin2a RNAi cells at 48–72 hpi using transmission electron microscopy (TEM) (Fig. 6B–D). Although cell morphology was dramatically perturbed, we observed infrequent gross structural anomalies in flagella and no FAZ defects (Fig. 6B,C). In wild-type and uninduced cells, we observed localization of IFT cargoes primarily on axoneme doublets 3–4 and 7–8, consistent with what was seen in PCF cells (Bertiaux et al., 2018a). In TbKin2a-silenced cells, 13% (*n*=55 images) had abnormal accumulations of material between the flagellar membrane and axoneme outer pairs 3–4 or 8–9 [the location of IFT cargo trains in *T. brucei* (Absalon et al., 2008)], whereas <3% (*n*=93 images) of control cells had such accumulations. Moreover, the nuclei of TbKin2a-silenced cells frequently displayed irregular shapes, areas of NE disorganization, and electron dense plaques of various sizes on the inner periphery of

Journal of Cell Science (2020) 133, jcs129213. doi:10.1242/jcs.129213

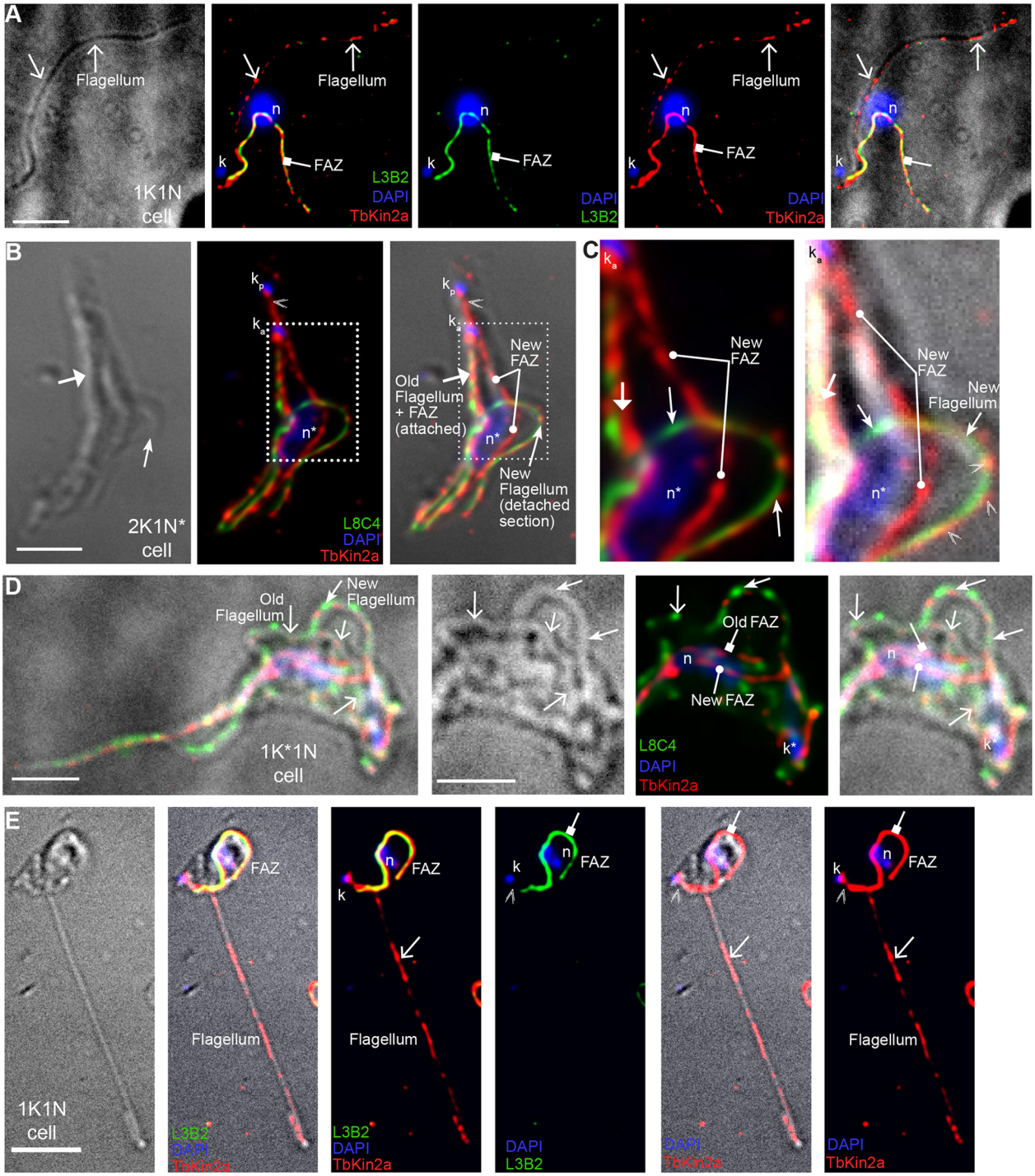

Fig. 4. TbKin2a localizes to the FAZ. (A) DIC and immunofluorescence images of 1K1N detergent-extracted cell stained for TbKin2a (red), FAZ marker protein TbFAZ1 (green, L3B2) and DNA (blue, DAPI). (B) 2K1N* cell, subjected to shear forces post-fixation but before mounting, such that the new flagellum has become partially detached from the cell body; stained for TbKin2a (red), flagellar PFR (green, L8C4) and DNA (blue, DAPI). Double V shows TbKin2a staining is continuous after initiating near the posterior kinetoplast. (C) Magnification of boxed area from B showing independent TbKin2a staining on the FAZ and on the detached flagellum. (D) 1K*1N cell, subjected to defined shear forces post-fixation such that both old and new flagella are partially detached from the cell body, stained for TbKin2a (red), flagellar PFR (green, L8C4), and DNA (blue, DAPI). (E) Cell grown in the presence of 5 mM EGTA plus 2 mM $MgCl_2$, in the 1K1N stage, with a single detached flagellum. The cell was stained for TbKin2a (red), FAZ marker protein TbFAZ1 (green, L3B2) and DNA (DAPI). Double V shows TbKin2a staining continuity between FAZ initiation point and basal body/kinetoplast. (A–E) Immunofluorescence images are 2D maximum intensity projections from 3D deconvolved *z*-stacks. Some abbreviations and symbols are from Fig. 2. New symbols: bar with filled square, interphase or old FAZ; bar with filled circle, new FAZ; wide arrow with filled arrowhead, unseparated flagellum and FAZ. Scale bars: 2.5 µm (A,E); 3 µm (B,D).

the NE (Fig. 6C,D). The plaques were similar in number and location to chromatin plaques observed at the periphery of nuclei in *T. brucei rhodesiense*, beginning in late mitosis and persisting into interphase (Farr and Gull, 2012; Vickerman and Preston, 1970). This ultrastructural evidence is consistent with the conclusion that TbKin2a plays a role in IFT and suggests that it

Journal of Cell Science (2020) 133, jcs129213. doi:10.1242/jcs.129213

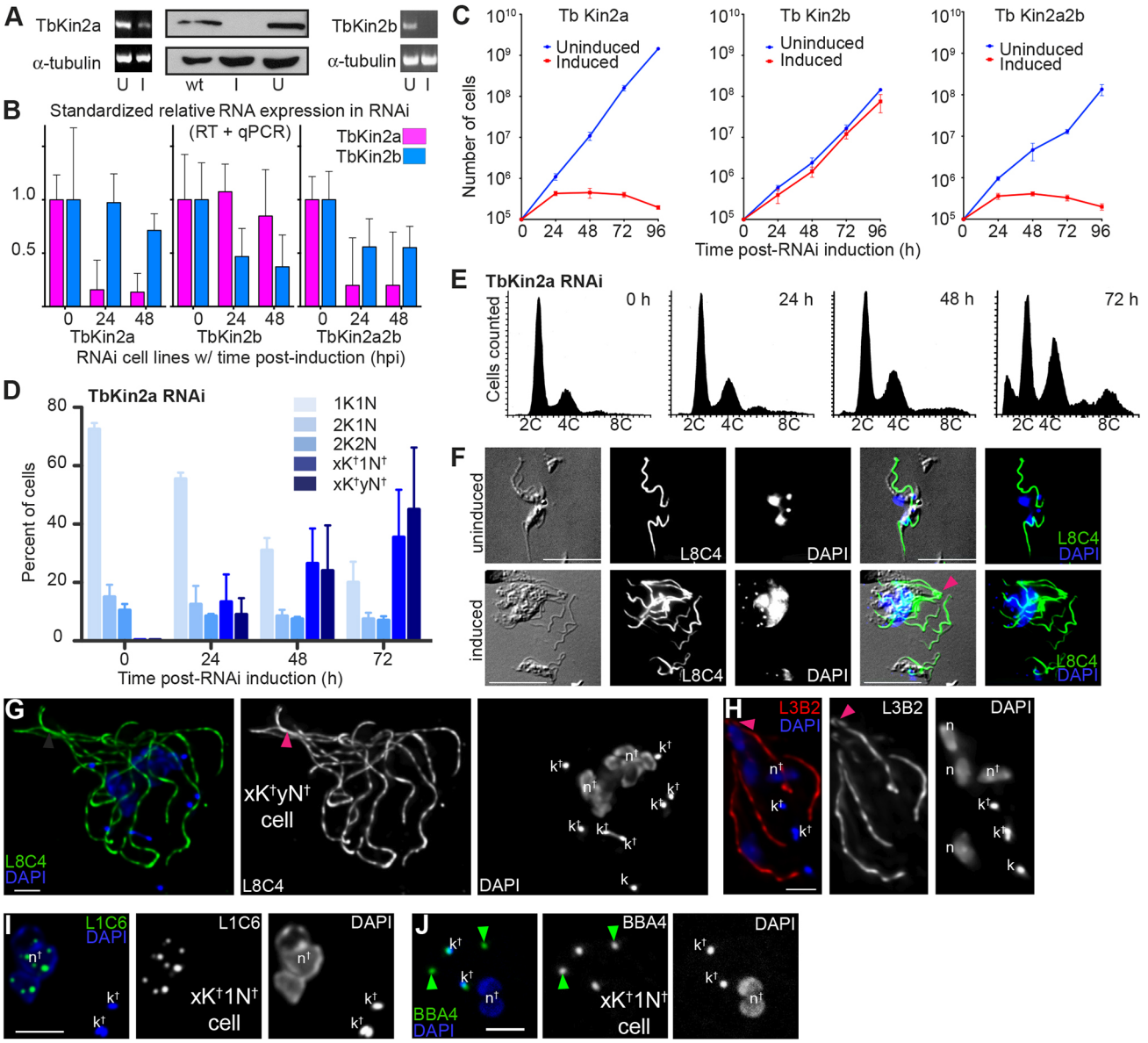

Fig. 5. Effect of RNAi silencing of TbKin2a and TbKin2b on cell proliferation and division. (A) Left and right: TbKin2a and TbKin2b mRNA levels in RNAi-uninduced (U) and RNAi-induced (I) cells at 48 hpi by RT-PCR, with α-tubulin mRNA levels as a control. Center: TbKin2a protein levels in wild-type (wt), RNAi-induced (I), and uninduced (U) cells at 48 hpi as assessed by western blotting using anti-TbKin2a (top) or anti-tyrosinated-α-tubulin YL1/2 (control) antibodies. (B) Comparison of uninduced versus induced normalized relative TbKin2a and TbKin2b mRNA levels in TbKin2a-silenced, TbKin2b-silenced and TbKin2a2b-silenced cells. For each RNAi cell line, induced and uninduced, data are from two independent experiments with three technical replicates. Error bars, s.d. Relative gene expression and s.d. was determined using the $2^{-\Delta\Delta CT}$ method. (C) Cell number versus hpi for cells uninduced or induced for RNAi to silence TbKin2a, TbKin2b or TbKin2a2b. Data are from two independent experiments, each with three technical replicates. Error bars, s.d. (D) Cell morphology phenotypes with nucleus (N) and kinetoplast (K) counts for TbKin2a RNAi uninduced (n=197 cells) and induced (n=230 cells) 0-72 hpi. 1†N, single abnormally large nucleus. Error bars, s.d. (E) FACS plots of DNA content for TbKin2a RNAi cells at 0–72 hpi. (F) DIC and immunofluorescence images of uninduced (top) or induced (bottom) cells at 72 hpi, stained for the PFR (green, L8C4) or DNA (blue, DAPI). (G) TbKin2a-silenced cells at 48 hpi stained as in F. (H) TbKin2a-silenced cell that was detergent-extracted and stained for the FAZ (red, L3B2) and DNA (blue). (I) TbKin2a-silenced cell at 72 hpi stained for DNA (blue, DAPI) and for nucleoli (green, L1C6). (J) TbKin2a2b-silenced cell at 72 hpi stained for DNA (blue, DAPI) and basal bodies (green, BBA4). (G–I) Immunoflourescence images are 2D maximum intensity projections from 3D deconvolved z-stacks. Arrowheads: red, bundled flagella (failed cytokinesis initiation); green, basal body abnormalities. Symbols: k†, abnormal or partially separated kinetoplast; N†, abnormal or unseparated nuclei. Scale bars: 10 µm (F); 5 µm (G); 2 µm (H–J).

may also play a role in late cell-cycle timing as well as NE and chromatin organization.

To measure the impact of TbKin2a and TbKin2b silencing on motility, we adapted a previously established sedimentation assay for PCF *T. brucei* in which the rate of sedimentation is inversely proportional to motility capacity (Bastin et al., 1999; Ralston and Hill, 2006). Sedimentation behavior was assessed over 4–8 h, beginning at 18 hpi, 24 hpi and 36 hpi. At 18–22 hpi, sedimentation rates for induced and uninduced cells were statistically equivalent (data not shown). However, after 24 hpi, cells silenced for TbKin2a or TbKin2a2b sedimented significantly faster than uninduced controls at every time point (Fig. 6E). In contrast, silencing TbKin2b alone did not result in faster sedimentation relative to controls. We conclude that TbKin2a silencing, but not TbKin2b silencing, results in a significant, progressive decrease in motility.

Journal of Cell Science (2020) 133, jcs129213. doi:10.1242/jcs.129213

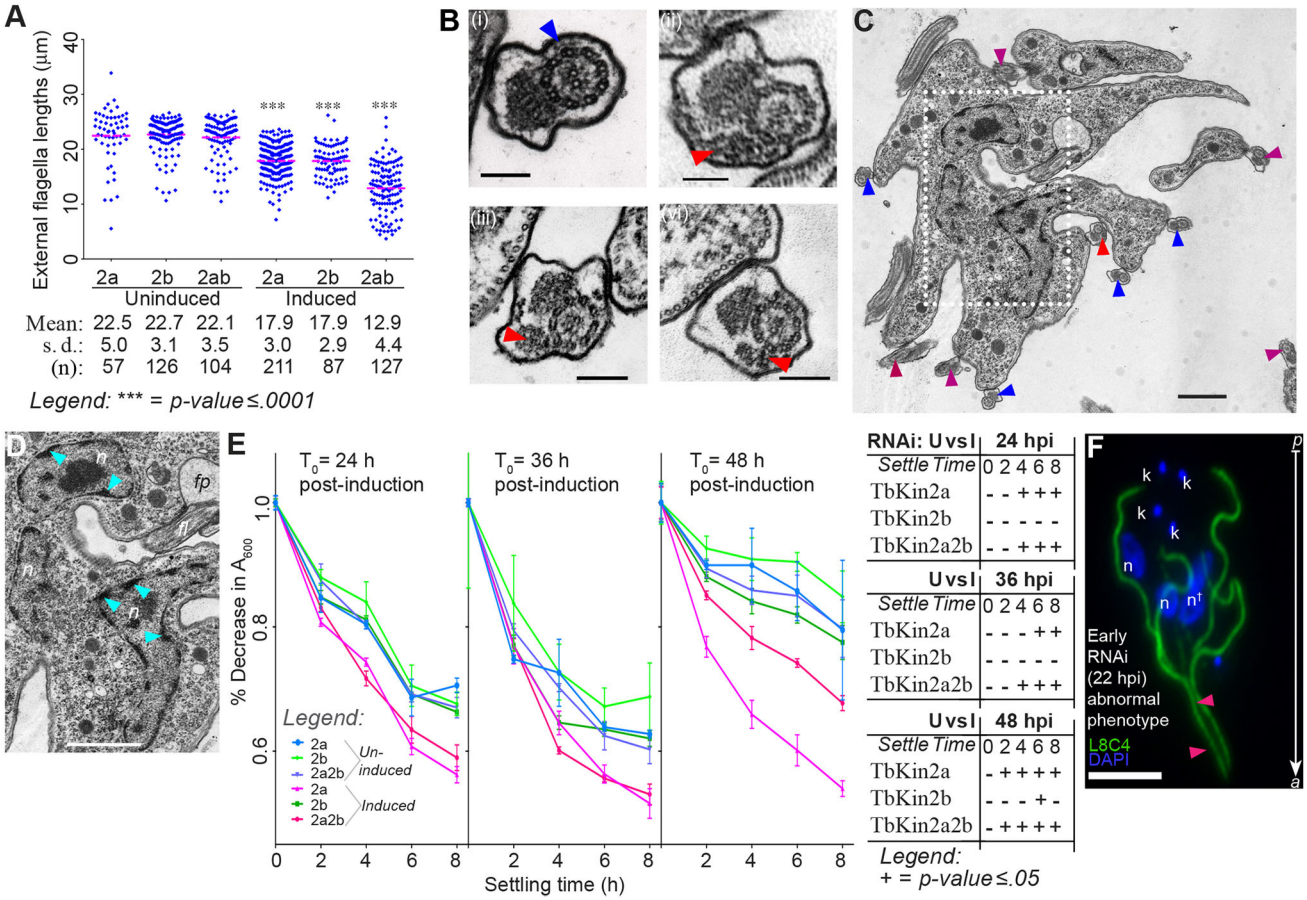

Fig. 6. Role of TbKin2a and TbKin2b in flagellar length and motility. (A) Flagellar length in uninduced cells (TbKin2a, *n*=57; TbKin2b, *n*=126; TbKin2a2b, *n*=104) and RNAi-induced cells (TbKin2a, *n*=211; TbKin2b, *n*=87; TbKin2a2b, *n*=127) at 48 hpi from three independent experiments. Mean, center line. Mean and s. d. are indicated in the table. One-way ANOVA with Sidak's multiple comparison tests using pooled variances was used to enable post-ANOVA comparisons of uninduced versus induced RNAi cell lines. ****P*<0.0001 (two-tailed test). (B) Transmission electron micrograph (TEM) of flagellar axonemes for control (i; blue arrow) and TbKin2a RNAi cells 48–72 hpi (ii–iv) showing IFT train deposition (red arrows). (C) TEM of a TbKin2a RNAi cell at 48–72 hpi. Blue arrows show apparently normal axonemes, red arrows show showing IFT train deposition, dark red arrows show axonemes not suitable to evaluate. (D) Magnified view of boxed area from C. Cyan arrowheads, DNA plaques at inner periphery of nuclear envelope. Symbols: n, nucleus; fp, flagellar pocket; fl, flagellum. (E) Sedimentation assays initiated at 24, 36 and 48 hpi for uninduced and induced samples of TbKin2a, TbKin2b and TbKin2a2b RNAi cell lines, with change in A_{600nm} at 0, 2, 4, 6 and 8 h settling times used to measure sedimentation rates. Data for 24, 36 and 48 h are each from one independent replicate with three technical replicates per sample. Dots, mean, error bars, s.d. Table shows the results of multiple unpaired *t*-tests, with one *t*-test per time point, with corrections for multiple comparisons using the Holm–Sidak method (+*P*<0.05; -, not significant). (F) Epifluorescence image of a TbKin2a-silenced cell at 20 hpi stained for the PFR (green, L8C4) and DNA (blue, DAPI), showing bundled anterior end flagella. Gray vertical arrow indicates anterior and posterior ends of cell. Symbols: k, kinetoplast; N, nucleus; N†, abnormal or unseparated nuclei; red arrowheads, bundled anterior-end flagella. Scale bars: 100 nm (B); 500 nm (C,D); 5 μm (F).

Finally, we evaluated the kinetics of onset of the TbKin2a RNAi phenotype by identifying abnormal cell morphologies as they formed over the first 26 hpi. We observed small numbers of abnormal cells beginning 16 hpi, and over the next 4–8 hpi abnormal cells accumulated such that, by 26 hpi, over 20% of the cell population had abnormal morphologies. The most frequent abnormal early phenotype observed was clustered or bundled flagella at the anterior cell end within abnormally large cells (Fig. 6F). Thus, the earliest phenotype associated with silencing TbKin2a is an apparent failure to initiate cytokinesis.

DISCUSSION

Kinesin-2 proteins perform an important and conserved function in IFT and flagellar biogenesis of primary and motile cilia (Lechtreck, 2015; Prevo et al., 2017; Scholey, 2013). Kinesin-2 proteins have also been implicated in bidirectional ER to Golgi transport (Brown et al., 2014; Stauber et al., 2006), endosomal trafficking (Granger et al., 2014), transport in neurons (Hirokawa et al., 2010), cilium-based signaling (Goetz and Anderson, 2010), chromosome segregation (Haraguchi et al., 2006; Miller et al., 2005) and cytokinesis completion (Brown et al., 1999; Fan and Beck, 2004). Here, we report that the kinesin-2 proteins TbKin2a and TbKin2b in BSF *T. brucei* function in flagellar biogenesis, but only TbKin2a appears to be crucial for cell proliferation. In addition, TbKin2a is found on the FAZ, suggesting a possible role in FAZ-based transport. Thus, kinesin-2 proteins in trypanosomes are likely to perform both canonical and trypanosome-specific roles.

Trypanosome kinesin-2 proteins have divergent NST sequences

The results of our MEME analysis complements previous kinesin bioinformatics studies (Berriman et al., 2005; Wickstead et al., 2010a) by identifying conserved sequence motifs in the non-motor-domain NST portions of kinesin-2 proteins. Unexpectedly, we found that kinesin-2 proteins contain over 20 conserved NST motifs, with several key motif groups, and are broadly shared across

Journal of Cell Science (2020) 133, jcs129213. doi:10.1242/jcs.129213

all superfamilies of flagellated eukaryotes. Several of these motifs had been previously recognized within a narrower phylogenetic context (De Marco et al., 2001; De Marco et al., 2003; Doodhi et al., 2009; Imanishi et al., 2006; Vukajlovic et al., 2011), while others, in particular NST motifs specific to subgroups 2A, 2B and 2C, appear to be new. Some motifs and motif groups were common to almost all taxa encoding kinesin-2, while others were specific for the taxa encoding heterotrimeric kinesins 2A and 2B or the homodimeric kinesin 2C.

Although the IFT machinery is highly conserved within the kinetoplastids (van Dam et al., 2013), it was surprising that the kinetoplastid taxa did not share common kinesin-2 NST motif groups and had little evidence of conserved individual motifs (Fig. S2). Kinetoplastids are also the only kinesin-2-containing organisms identified that do not encode non-motor KAP homologs in their genomes (Julkowska and Bastin, 2009). The free-living kinetoplastid *B. saltans* also does not encode a KAP homolog, suggesting that it was not lost as a result of parasitism. Our MEME analysis and KAP genomic data do not support bioinformatic assignment of kinetoplastid kinesin-2 proteins as orthologs of the canonical heterotrimeric kinesin-2A or 2B forms. However, a kinetoplastid kinesin-2 protein did share a single significant kinesin-2C motif with those found in Metazoa, which was the sole example of a homodimeric kinesin-2C motif among non-holozoan single-celled organisms. Together with the markedly different phenotypes caused by TbKin2a versus TbKin2b RNAi silencing in BSF *T. brucei*, these data suggest that kinesin-2 proteins in *T. brucei* do not form canonical heterotrimers. Instead, the kinetoplastid kinesin-2 proteins represent a distinct subgroup that differ significantly in sequences and motifs, may form homodimers or heterodimers, and may differ in function compared with kinesin-2 proteins in other organisms.

Trypanosome kinesin-2 proteins are important for flagellum biosynthesis

We found that silencing TbKin2a or TbKin2b results in a ∼20% decrease in flagellum length, while silencing both causes a decrease of 40% (although flagella are present). Moreover, TbKin2a localizes along the flagellum, with a concentration on basal bodies and the proximal flagellum, similar to the localization of the *Chlamydomonas reinhardtii* kinesin-2 FLA10 (Cole et al., 1998; Deane et al., 2001; Vashishtha et al., 1996). TbKin2a also colocalizes with both the IFTB protein IFT172 and IFTA protein IFT144 near basal bodies. Silencing TbKin2a decreased staining of both IFT172 and IFT144 on the flagellum and decreased the localization of IFT144, but not IFT172, to the basal body. Moreover, flagella in TbKin2a-silenced cells showed accumulation of electron-dense material along axonemes, but otherwise did not show gross abnormalities. [We could not always resolve fine structural elements such as inner dynein arms, which require kinesin-2 for transport in *C. reinhardtii* (Piperno and Mead, 1997; Piperno et al., 1996).] These data suggest that TbKin2a and TbKin2B participate in IFT.

One distinction between TbKin2a and TbKin2b that is of potential significance is the presence of a putative C-terminal nuclear localization signal (NLS) sequence in TbKin2a, but not in TbKin2b [NLS predicted using NucPred (Brameier et al., 2007) and MultiLoc2 (Blum et al., 2009)]; this sequence might also function as a ciliary localization signal sequence (CLS) (Verhey et al., 2011). For the homodimeric kinesin-2 protein KIF17, an NLS/CLS mediates entry into the ciliary compartment (Dishinger et al., 2010; Kee et al., 2012). Thus, TbKin2a and TbKin2b may play different roles in cargo entry into flagella. Investigations in *C. elegans* indicate that heterotrimeric kinesin-2A/2B is primarily responsible for cargo entry into the flagellum transition zone. Following cargo entry, kinesin-2A/2B gradually undocks while homodimeric kinesin-2C docks in the proximal segment. Finally, kinesin-2C becomes the primary transport motor in the distal segment (Prevo et al., 2015). By analogy, TbKin2a and TbKin2b may play different roles in cargo transport at different flagellar regions.

In many other organisms, kinesin-2 proteins are essential for flagellum biogenesis and maintenance (Lechtreck, 2015; Prevo et al., 2017; Scholey, 2013). However, in BSF *T. brucei*, silencing kinesin-2 proteins resulted in partial but not complete inhibition of flagellum biosynthesis and maintenance. This may be due to incomplete RNAi silencing, slow protein turnover, the presence of other kinesins with redundant roles or increasingly pleiotropic effects of RNAi over time or other processes in BSF cells such as cell cycle progression, which result in cell death before flagellar shortening is complete (Blaineau et al., 2007; Broadhead et al., 2006; Chan and Ersfeld, 2010; Demonchy et al., 2009; Marande and Kohl, 2011; Wickstead et al., 2010b). Interestingly, in PCF *T. brucei* IFT is active in both new and old flagella, but silencing either anterograde IFTB or retrograde IFTA components causes a failure in new flagellum biosynthesis (although with somewhat different phenotypes) but no defect in old flagellum maintenance (Fort et al., 2016). Another recent study demonstrated that individually silencing TbKin2a or TbKin2b had no effect on flagellum length in PCF, but silencing both caused shorter flagella (Bertiaux et al., 2018a), suggesting a redundant function in IFT. Our results are consistent with both individual and redundant roles for kinesin-2 proteins in anterograde IFT during new flagellum biosynthesis in BSF *T. brucei*.

TbKin2a is essential for cell proliferation

Interestingly, silencing TbKin2a expression caused a cessation of cell proliferation beginning at ∼24 hpi, whereas silencing TbKin2b expression had no apparent effect on cell proliferation. Silencing TbKin2a also caused a failure in cytokinesis, with the accumulation of enlarged cells with multiple nuclei, kinetoplasts, basal bodies, FAZ and flagella, as well as decreased cell motility. It is surprising that only TbKin2a is important for proliferation, cytokinesis and motility, although both TbKin2a and TbKin2b contribute to flagellar length. This suggests that cells can withstand flagellar length decreases of at least 20%, and that shorter flagella in BSF cells can be functional, perhaps through a compensatory mechanism such as decreased cell size, as in PCF *T. brucei* (Kohl et al., 2003).

The cell proliferation defects caused by silencing TbKin2a in BSF cells are similar to the defects caused by RNAi silencing of other flagellar proteins, FAZ proteins and basal body proteins (Broadhead et al., 2006; LaCount et al., 2002; Morris et al., 2001; Ralston et al., 2006), as well as cell-cycle-related proteins, signaling proteins and cell surface proteins (Farr and Gull, 2012; Hammarton et al., 2007b). The commonality of phenotypes is specific to BSF cells and may be due to the fact that silencing these factors directly or indirectly impacts cytokinesis (Hammarton et al., 2007b; Hughes et al., 2013; Oberholzer et al., 2011; Wheeler et al., 2013; Zhou et al., 2014).

It has been hypothesized that cell proliferation and cytokinesis defects in BSF trypanosomes can result from inhibited flagellar beating (Broadhead et al., 2006; Ralston et al., 2006). However, defects in flagellar beating may not explain the cell proliferation and cytokinesis phenotypes observed in TbKin2a-silenced cells for several reasons. First, normal flagellar beating is not essential for cytokinesis, because the cell proliferation and cytokinesis defects caused by silencing dynein light chain 1 by RNAi can be rescued by the expression of site-specific mutants that are still defective in

flagellar motility (Kisalu et al., 2014; Ralston et al., 2011). Second, silencing TbKin2a did not cause gross ultrastructural abnormalities in flagella or the flagellar pocket other than abnormal IFT train accumulation, in contrast to the major defects caused by silencing other flagellar proteins (Broadhead et al., 2006; Farr and Gull, 2009). Third, we find that following TbKin2a RNAi induction, the kinetics of onset of the cytokinesis defect precedes the defect in cell motility. For example, at 16–20 hpi, abnormal cells with bundled flagella and FAZ at their anterior ends are observed, suggesting a defect in cytokinesis initiation. Abnormal cells are also observed connected at their posterior ends, suggesting a defect in cell scission. At 24 hpi, cell proliferation is affected, and there is a decrease in motility thereafter, although the flagella in the abnormal cells continue to beat. These considerations suggest that TbKin2a may play a role in cytokinesis initiation that is independent of any role in flagellar motility. This may be due to its involvement in transporting cargoes into flagella that themselves are important for cytokinesis or its presence on the FAZ, as discussed below.

Implications of TbKin2a localization on the FAZ

It is intriguing that TbKin2a also localizes to the FAZ. However, TbKin2a does not appear to be important in the construction, maintenance or structure of the FAZ because we did not observe abnormalities in the FAZ or flagellar detachment in TbKin2a- or TbKin2a2b-silenced cells. Instead, we propose that TbKin2a interacts with the FAZ via the MtQ and may transport other cargoes or facilitate intracellular signaling, including those essential for cell division. This is the simplest model, given the ability of TbKin2a to bind to microtubules, and that TbKin2a staining is present between the basal body and FAZ initiation site in the same location as the MtQ (Lacomble et al., 2009, 2010). Because MtQ microtubules are uniformly oriented with their plus ends towards the cell anterior (Gull, 1999), antiparallel to the remainder of the subpellicular array (Robinson et al., 1995), they represent a potential track for moving cargoes along the anterior–posterior cell axis.

We speculate that cargoes transported by TbKin2a along the FAZ could include both organelles and cell cycle regulatory molecules. The FAZ is linked with other single-copy structures including the kinetoplast, tripartite attachment complex (TAC), basal body, flagellum, flagellar pocket collar, and bilobe structure with ER and Golgi exit sites (Gadelha et al., 2009; Gheiratmand et al., 2013; Gluenz et al., 2011; Lacomble et al., 2009, 2010; Sunter et al., 2015; Zhou et al., 2015). TbKin2a may be involved in transporting components involved in these interactions. For example, basal bodies and kinetoplasts are connected by the TAC (Ogbadoyi et al., 2003), and basal body duplication and separation are necessary for kinetoplast segregation (Robinson and Gull, 1991). We observed defects in kinetoplast separation and basal body to kinetoplast attachment in TbKin2a-silenced cells, suggesting that TbKin2a may participate in TAC assembly or maintenance. TbKin2a may also be important for the transport of structural or regulatory proteins that are important for cell cycle regulation as well as duplication and segregation of many of the above-mentioned components, which include the centrins 1, 2 and 4 (Selvapandiyan et al., 2007; Shi et al., 2008; Wang et al., 2012), as well as polo-like kinase (TbPLK) (de Graffenried et al., 2008, 2013; Ikeda and de Graffenried, 2012; Li et al., 2010; Umeyama and Wang, 2008). Notably, TbPLK is transported along the MtQ to the anterior tip of the cell (Ikeda and de Graffenried, 2012; Li et al., 2010; Sun and Wang, 2011; Yu et al., 2012), where it is required for cytokinesis initiation (Hammarton et al., 2007a; Kumar and Wang, 2006). Recent studies have also identified new proteins that are associated with the FAZ and control various aspects of *T. brucei* cytokinesis (Hilton et al., 2018; Sinclair-Davis et al., 2017; Zhang et al., 2019; Zhou et al., 2018). Future experiments will be aimed at determining whether TbKin2a and TbKin2b transport distinct cargoes along the flagellum and/or FAZ, and how cargo transport contributes to flagellum construction, organelle transport and positioning, and cytokinesis.

MATERIALS AND METHODS

MEME suite analysis

Multiple EM for Motif Elicitation (MEME) web-based software (Bailey and Elkan, 1994; Bailey and Gribskov, 1998; Bailey et al., 2006, 2009) (versions 3.91-4.11) was used to analyze the NST domains of putative kinesin-2 proteins. Using taxa encoding kinesin-2 identified in a phylogenetic analysis of kinesin motor domain sequences from 45 diverse organisms (Wickstead et al., 2010a) as the starting point, we carried out more than 80 independent MEME computational runs including multiple combinations of kinesin-2 NST data subsets and input parameters with multiple controls. See Table S3 for a reconciliation of kinesin-2 sequences used in our MEME NST analyses with and kinesin-2 sequences used in a prior motor domain analysis (Wickstead et al., 2010a). To ensure that all NST domains consistently included a full neck region, which has been shown to evolve independently of the motor domain (Case et al., 2000; Vale and Fletterick, 1997), our NST domain for each taxon began with the final three amino acids (positions 343–345) of the PFAM-defined motor domain sequence specification (PFAM00225). MEME results were sensitive to changes in inputs and assumptions including composition, length and number of protein sequences, expected motif distribution and run parameters. To overcome this sensitivity, many runs of kinesin-2 sequences, as well as control sequences, were conducted until consistent result patterns were observed. Our controls included running a full MEME analysis of: kinesin-1 family NST sequences; kinesin-1, -3 and -4 family neck domain sequences; kinetoplastid and non-kinetoplastid kinesin NST sequences; and scrambled kinesin-2 NST sequences (NST sequences are found in Table S4). Overall results were generally robust and consistent but as already noted, could vary from run to run. Kinesin-2 NST motif results presented here are from a single run (MEME 83) that we judged to be highly consistent with overall result patterns from about eight final MEME runs. All MEME statistics presented were generated by standard MEME programs (Bailey and Elkan, 1994; see Figs S1, S2, Table S3).

Cell culture and RNA interference

BSF *T. brucei brucei* Lister 427-derived cell line 90-13 (Wirtz et al., 1999) was cultured and maintained in HMI-9 media. Media was initially supplemented with 10% Serum Plus (MilliporeSigma, Burlington, MA) and 10% tetracycline-tested, heat-treated fetal bovine serum (FBS) (R&D Systems, Minneapolis, MN), and later supplemented with 15–20% FBS only (complete medium), as otherwise described previously (Li and Wang, 2006; Tu and Wang, 2004), with splitting of the cultures at final densities of $\sim 1.0\times10^6$ cells/ml. For RNAi, DNA corresponding to the 380-bp *T. brucei* gene Tb927.5.2090 (TbKin2a) or the 462-bp gene Tb927.11.13920 (TbKin2b) (selected using RNAit software; Redmond et al., 2003) were amplified by PCR from genomic DNA (primers listed in Table S5). For RNAi of TbKin2a or TbKin2b, PCR fragments were ligated into the XhoI and HindIII sites of pZJM (Wang et al., 2000). For RNAi of both TbKin2a and TbKin2b, the TbKin2b PCR product was ligated into the XbaI and XhoI sites in pZJM that already contained TbKin2a. All DNA sequences were verified. Transfections (Burkard et al., 2007; Li and Wang, 2006) and selection of monoclonal transformants were performed using agarose plates as described previously (Carruthers and Cross, 1992; Tan et al., 2002). For induction of RNAi, monoclonal transformants were cultured with 1 µg/ml tetracycline for 0-96 h as indicated. For growth curves, live cells were counted using a hemocytometer.

Antibody generation

A portion of the TbKin2a gene encoding amino acids 391–696 plus a C-terminal 6×His tag (TbKin2a.391-696-His) was amplified by PCR using primers listed in Table S5, ligated into the NcoI and NotI sites in pET22b(+)

(Novagen, Madison, WI), and verified by DNA sequencing. Recombinant TbKin2a.391-696-His was expressed in *E. coli* BL21-CodonPlus-RP cells (Agilent Technologies, Cedar Creek, TX) after induction with 400 µM IPTG at 37°C for 2 h. The protein was purified by Ni-NTA (Qiagen, Valencia, CA) affinity chromatography followed by gel filtration chromatography on a Superdex 75 column (GE Healthcare, Piscataway, NJ). To generate anti-TbKin2a antibody, rabbits were immunized by Covance Inc. (Princeton, NJ) using purified TbKin2a.391-696-His. Antibody was affinity purified using standard procedures.

Engineering *T. brucei* to express TbKin2a–Myc

To generate a *T. brucei* strain expressing Myc-tagged TbKin2a under the control of its endogenous promoter, we used the long primer PCR transfection method described for C-terminal fusion protein expression in bloodstream form *T. brucei* (Dean et al., 2015), except that plasmid pPOTv7 was used as template DNA for PCR amplification. pPOTv7 encodes a 10× Myc tag at the C-terminus and the blasticidin resistance *bsr* gene, rather than the hygromycin resistance *hpt* gene that is in pPOTv4. For forward long primer, we used final 80 nucleotides prior to the stop codon of the Tb927.5.2090 gene, followed in frame by the applicable 18 nucleotide pPOTv4/v7 annealing sequence (5′-GGTTCTGGTAGTGGTTCC-3′). For the reverse primer, we used the reverse complement of the first 80 nucleotides (without stop codon) of the 3′ untranslated region of Tb927.5.2090 gene followed in frame by the reverse complement form of the applicable 20 nucleotide pPOTv4/v7 annealing sequence (5′-CCAATTTGAGAGACCTGTGC-3′). Primers were synthesized by Integrated DNA Technologies (Coralville, IA). PCR was performed using Phusion HF DNA Polymerase (New England BioLabs, Ipswich, MA). The DNA sequence of the PCR products was confirmed. PCR products were ethanol precipitated and resuspended in water. For electroporation of *T. brucei* BSF 90-13 we used the AMAXA Nucleofector (Lonza, Basel, Switzerland) with program X-001 for BSF *T. brucei*, as specified in Burkard et al. (2007), except that we used the transfection buffer specified in Schumann Burkard et al. (2011). *T. brucei* cells were cultured at 37°C in HMI-9 medium containing 10% (v/v) heat-inactivated fetal bovine serum, with 2.5 µg/ml neomycin and 5 µg/ml hygromycin. After transfection, the cells were selected by serial dilution with the addition of blasticidin at 10 µg/ml.

Western blotting

For western blotting of cell lysates from wild-type BSF 90-13 cells and TbKin2a RNAi (induced and uninduced) cells, whole-cell lysates were boiled in 1× SDS loading buffer (200 mM Tris-HCl pH 6.8, 8% SDS, 0.3% Bromophenol Blue, 30% glycerol and 15% β-mercaptoethanol), separated by SDS-PAGE, and transferred to a nitrocellulose membrane. After a 1 h blocking step in TBS-T (20 mM Tris pH 8.0, 150 mM NaCl, 0.02% Tween 20) with 5% dry milk, membranes were incubated with primary antibodies in TBS-T plus 5% dry milk as follows: affinity-purified anti-TbKin2a antibody at a dilution of 1:10,000; YL 1/2 rat monoclonal anti-tyrosylated α-tubulin antibody (cat. no. MAB1864-I, MilliporeSigma, Burlington, MA) at a dilution of 1:100; KMX mouse anti-β-tubulin antibody (Birkett et al., 1985) at a dilution of 1:100. After three washes in TBS-T+5% dry milk, the membrane was incubated with applicable anti-rabbit, anti-rat or anti-mouse-IgG secondary antibodies conjugated to horseradish peroxidase (Thermo Fisher Scientific) at the manufacturer recommended dilutions and washed twice for 10 min in TBS-T plus 5% dry milk and twice for 5 min in PBS (137 mM NaCl, 2.7 mM KCl, 10 mM Na_2HPO_4, 2 mM KH_2PO_4, pH 7.4), and then blots were imaged.

For BSF trypanosomes expressing TbKin2a–Myc, whole-cell protein lysates were prepared and subjected to SDS-PAGE as described above, and proteins were transferred to nitrocellulose membranes. After a 1 h blocking step in TBS-T plus 5% dry milk, membranes were incubated with primary antibodies in TBS-T plus 5% milk as follows: mouse anti-Myc 9E10 (Evan et al., 1985) at a dilution of 1:1000; rabbit anti-TbKin2a at a dilution of 1:10,000. After three washes in TBS-T plus 5% dry milk, the membranes were incubated with secondary antibodies as follows: Alexa Fluor 680 anti-mouse-IgG (ThermoFisher Scientific, Waltham, MA) and AlexaFluor 790 anti-rabbit-IgG (ThermoFisher Scientific), both at 1:10,000 dilution. Membranes were washed twice in TBS-T plus 5% dry milk and twice for 5 min in PBS. Blots were imaged using the Odyssey infrared imaging system (Li-Cor Biosciences, Lincoln, NE).

RT-PCR and qRT-PCR

For all RT-PCR and qRT-PCR studies, total RNA (from at least two independent biological replicates) was extracted and isolated individually for each experiment from freshly spun-down, unwashed *T. brucei* BSF RNAi cells (induced or uninduced) using either TRI Reagent or RNAzol [Molecular Research Center (MRC), Cincinnati, OH]. RNA for semi-quantitative RT-PCR was purified after isolation using MRC RNA precipitation protocols, including a DNase treatment step using TurboDNAse (Thermo Fisher Scientific). For qRT-PCR from RNAi cells, RNA extracted and isolated as above from n=2 (TbKin-2a), n=2 (TbKin2b), and n=2 (TbKin2a2b) independent biological replicates was individually purified either as above, or by immobilizing extracted and isolated RNA on silica columns [Direct-zol, Zymo Research (ZR), Carlsberg, CA], treating with DNase, and purifying, all as described in the manufacturer's protocols (except that an additional wash step of 100% ethanol was included) and as a final step, eluted with pure DEPC water. Purified RNA in DEPC water was analyzed using a Nanodrop spectrophotometer (ThermoFisher Scientific) and stored at −80°C. For qRT-PCR, purified RNA integrity for each sample was confirmed (Schroeder et al., 2006) using an Agilent Bioanalyzer 2100 (Agilent Technologies, Santa Clara, CA) by the UC Berkeley QB3 Functional Genomics Laboratory. All primers were from Integrated DNA Technologies (Coralville, IA). For semi-quantitative RT-PCR, first-strand cDNAs were generated from RNA using SuperScript III First-Strand Synthesis System (ThermoFisher Scientific) with oligo(dT) primers, and PCR was performed using first-strand cDNA and with gene-specific primers. qRT-PCR used a two-step procedure with first-strand cDNAs generated from purified RNA using a Superscript VILO cDNA Synthesis Kit (ThermoFisher Scientific). We evaluated *T. brucei* potential reference standard genes as recommended previously (Brenndörfer and Boshart, 2010). Only one gene, TERT (telomerase reverse transcriptase, Tb927.11.10190), had minimal expression variation under our experimental conditions and was selected as sole reference standard. All qRT-PCR work was performed in 96-well plates using either Applied Biosystems (ABI) 7500 Fast Real-Time PCR System and iTaq SYBR Green Supermix (ThermoFisher Scientific); or Roche LightCycler96 System using iQ SYBR Green Master Mix (Bio-Rad, Inc., Richmond, CA) using separate wells for reference and target reactions. Gene-specific primers for qRT-PCR were designed using ABI Primer Express Version 2.0 software and/or Primer3 software (Untergasser et al., 2012) and sequences are in Table S5. Amplification efficiency of each gene/primer combination was confirmed over a 4- to 5-log dilution series. Relative gene expression for qRT-PCR was determined for each biological experiment, and results were aggregated using the $2_T^{-\Delta\Delta C}$ method (Schmittgen and Livak, 2008).

Fluorescence-activated cell sorting

Cell samples for fluorescence-activated cell sorting (FACS) were prepared as described previously (Tu and Wang, 2004). FACS was carried out using an Epics XL flow cytometer (Beckman Coulter, Brea, CA). Data were analyzed using FlowJo 4-5 software (FlowJo LLC, Ashland, OR; a subsidiary of Becton, Dickinson and Company).

Motility assays

At experiment initiation, cells were centrifuged and transferred to 1–10 ml of fresh settling medium [a 1:1 (v/v) mix of heat-treated tetracycline-free fetal bovine serum (R&D Systems, Minneapolis, MN) and regular complete HMI-9 medium (Engstler et al., 2007)] at starting densities of ∼0.5×10^5–3×10^5 cells/ml, with or without tetracycline at 37°C with 5% CO_2. Using previously described methods, including centrifuging live cells and replacing medium at 12–24 h intervals (Hesse et al., 1995), uninduced and induced cells were grown in settling medium for up to 48 h and reached final densities of up to∼5×10^6 cells/ml. At 18, 24, 36 and 48 h after growth in the settling medium and RNAi induction, cells were counted and 1 ml of cells was transferred into each of three grouped cuvettes per cell line (uninduced and induced) and sealed with sterile, liquid impermeable and gas-permeable film. Cuvettes were agitated and the initial A_{600nm} at 0 min

Journal of Cell Science (2020) 133, jcs129213. doi:10.1242/jcs.129213

was measured using a SpectraMax M2 multi-detection reader (Molecular Devices, Sunnyvale, CA) or Genesys 10 spectrophotometer (Thermo Fisher Scientific, Waltham, MA). Cuvettes were incubated at 37°C with 5% CO_2, and at each subsequent time point (every 1–2 h up to 8 h), cuvettes were removed from the incubator. A_{600nm} measurements were obtained and changes in absorbance were calculated.

Methods for separating flagella from FAZ

For controlled shearing of flagella from cell bodies, we devised a simple parallel-plate flow chamber device and shearing procedure to apply measured, consistent shear forces. 24×40 mm poly-L-lysine-coated #1.5H high-precision coverslips (Paul Marienfeld GmbH & Co. KG, Lauda-Königshofen, Germany) were pre-weighed dry, then fully fixed cells (see staining for fluorescence microscopy) were added, coverslips were mounted onto a cleaned glass slide with 50–120 µl ProLong Gold antifade (Invitrogen), and the assembly was placed into a mounting slot in the device base, which had been levelled and clamped in place and maintained at room temperature. Coverslips were re-weighed after each step above. A 25×50 mm glass slide top-plate, with or without attached weights (total top plate mass as used was 7.55–10.52 g), was loaded carefully onto the coverslip, flush along the back side, between device guides. All masses were determined using a single, calibrated, fully-enclosed Mettler Toledo AB54-S analytical balance. Using a stopwatch and pusher rod placed directly at the back of the coverslip, the coverslip and top plate assembly was pushed by hand in a single direction at an approximately constant velocity of ∼0.7–1 mm/s for 4–5 s over a measured distance of ∼4–5 mm. Immediately before and after the above-mentioned steps, clean, dry pre-weighed Kimwipes (Kimberly-Clark, Roswell, GA) held in micro-forceps were used to blot-up excess liquid and immediately reweighed, with all before and after wipe masses recorded and weights adjusted. Shear-treated coverslips were then allowed to set in dark at 4°C for 24 h, then sealed as described in the section below.

It was previously noted that BSF *T. brucei* cells grown in citrated blood to chelate Ca^{2+} resulted in cells with attached parent flagella but detached daughter flagella (Vickerman, 1969). Based on this observation, we developed a simple procedure in which BSF cells were cultured for 18–30 h at 37°C in HMI-9 complete medium supplemented with either 5–20 mM sodium citrate or 2.5–10 mM EGTA to chelate Ca^{2+}, and 1–5 mM $MgCl_2$ (Oberholzer et al., 2011). Under these conditions, many cells had detached flagella, including a subset of 1K1N cells that had a full-length FAZ as demonstrated by L3B2 staining, and had the sole flagellum detached from the cell body except at the flagellar base. Live cells in medium were settled on coverslips for fixation and staining as described below.

Staining for fluorescence microscopy

Except for counts of nuclei/kinetoplast morphology, for all immunofluorescence microscopy, live cells were either (i1) centrifuged at 500–1200 ***g*** for 5–14 min to concentrate and diluted in 37°C fresh HMI-9 complete medium or HBS/G (25 mM HEPES pH 7.1, 140 mM NaCl, 5 mM KCl, 0.75 mM Na_2HPO_4, 22 mM glucose) to 1.5–2.0×10^6 cells/ml, or (2) cells at 0.8×10^6–1.2×10^6 cells/ml were settled directly onto coverslips (#1.5H high precision-type; Paul Marienfeld GmbH & Co. KG) coated with poly-L-lysine (Amanda Polymers, Birmingham, AL) for 20–40 min. For formaldehyde-only fixation, cells on coverslips were washed once or twice in HBS/G, then fixed immediately in HMI-9 complete medium, or HBS/G buffer, at 37°C with freshly added formaldehyde (Ted Pella, Inc.) to 0.75% to 4% final concentration for 10–30 min at room temperature. For formaldehyde plus methanol fixation, cells on coverslips were washed once or twice in HBS/G, then fixed immediately in HMI-9 complete medium, or HBS/G buffer, at 37°C with freshly added formaldehyde (Ted Pella, Inc.) to 0.50% to 1% final concentration for 7–15 min at room temperature. Coverslips were then washed two or three times in HBS/G, placed on ice, and fixed with −20°C methanol for 15–30 min. Fixation was followed by three to five washes in cold PEME (100 mM PIPES pH6.9, 2 mM EGTA, 1 mM Mg_2SO_4, 0.1 mM EDTA) (Robinson et al., 1991) and a 10–20-min rehydration in cold PEME. For methanol-only fixation (including flagellar length or intensity measurements), cells on coverslips were washed twice in HBS/G, placed on ice and fixed in −20°C methanol for 10–40 min, followed by PEME washing and rehydration steps as above.

When used, detergent extraction was carried out before fixation on live unfixed cells at room temperature using the Nonidet P-40 in PEME buffer as described previously (Robinson et al., 1991), except that (1) live cells were settled onto and extracted on poly-L-lysine-coated coverslips; (2) IGEPAL CA-630 was substituted for Nonidet P-40 at 1% for 5 min at room temperature; and (3) cell extraction buffer and extracted cytoskeletons were stabilized in in HBS/G or PEME/G buffers supplemented with 2× cOmplete™ protease inhibitor cocktail, EDTA-free (Roche Diagnostics), plus 1 mM E 64d cysteine protease inhibitor (Apex Biotechnology, Taiwan). For extracted cells, buffers used prior to fixation were supplemented with 5 mM ATP (molecular biology grade; Millipore Sigma) and 2 mM $MgCl_2$ (except as noted below for cells expressing TbKin2a–Myc).

Following fixation, non-extracted cells were permeabilized (for formaldehyde-only or formaldehyde plus methanol-fixed cells) were permeabilized in PEME plus 0.1% IGEPAL for 5–8 min and washed in PEME buffer. All fixed cells were blocked and incubated in primary then secondary antibodies in PEMEBALG [PEME plus 1% bovine serum albumin (BSA), 0.1% sodium azide, 100 mM lysine, 0.5% cold water fish skin gelatin solution (Millipore Sigma) plus normal goat serum] as described previously (Sagolla et al., 2006) at the following concentrations: L8C4 (Kohl et al., 1999), 1:100; KMX (Birkett et al., 1985), 1:25-1:50; L3B2 mouse anti-FAZ (Kohl et al., 1999), 1:10−1:100; YL1/2 (cat. no. MAB1864-I, MilliporeSigma, Burlington, MA), 1:100; BBA4 mouse monoclonal anti-basal-body (Woods et al., 1989), 1:50; L1C6 mouse anti-nucleolar protein (Durand-Dubief and Bastin, 2003), 1:200; mouse anti-IFT144 (PIFTF6) (Absalon et al., 2008), 1:200; mouse anti-IFT172 (Absalon et al., 2008), 1:1000; rabbit anti-TbKin2a (this study), 1:20,000. Secondary antibodies conjugated to Alexa Fluor 488 or Alexa Fluor 568 (Invitrogen) were diluted at 1:400, with DAPI at 1-10 µg/ml. For double staining with mouse anti-IFT172 and mouse L3B2, anti-IFT172 was labeled with Zenon Alexa Fluor 488 (Invitrogen) and used at a 1:1000 dilution, and L3B2 was labeled using Zenon Alexa Fluor 568 (Invitrogen) and used at 1:10, using the recommended Zenon protocol. Coverslips were mounted onto slides using ProLong Gold antifade and allowed to set hard in the dark at 4°C for at least 24 h, then sealed with clear nail polish before imaging.

For nuclei and kinetoplast morphology counts, 0.7×10^7–2.0×10^7 live cells were centrifuged, washed in PBS/G (PBS with 20 mM glucose), then fixed with 4% formaldehyde for 20–30 min. Fixed cells were isolated by centrifugation, washed in PBS, placed on poly-L-lysine-coated coverslips and post-fixed with −20°C methanol for 20–30 min. Fixed cells on coverslips were permeabilized and blocked in PBS with 1% BSA and 0.1% Triton X-100 for 1 h. For staining, cells were incubated with mouse anti-PFR L8C4 antibody (Kohl et al., 1999) at 1:50 in PBS with 1% BSA and then with Alexa Fluor 488 anti-mouse-IgG secondary antibody (Invitrogen) and DAPI (1–10 µg/ml). Samples were mounted using ProLong Gold antifade (Invitrogen) and allowed to set hard in the dark at 4°C for at least 24 h, then sealed with clear nail polish before imaging.

For cells expressing TbKin2a–Myc, transfected cells in medium were placed onto poly-L-lysine-coated coverslips, allowed to settle briefly, and washed in HBS/G. Cells were detergent-extracted using the Nonidet P-40 method in PEME/G as described previously (Robinson et al., 1991) and fixed in −20°C methanol, as noted above. HBS/G and PEME/G buffers were supplemented as noted above except that concentrations of ATP and $MgCl_2$ used were 10 mM and 4 mM, respectively. Cells were blocked and incubated in primary then secondary antibodies as described previously (Sagolla et al., 2006) at the following concentrations: L3B2 mouse IgG1 anti-FAZ monoclonal antibody (Kohl et al., 1999), 1:50–1:100; anti-Myc mouse IgG2a monoclonal antibody 9B11 (Cell Signaling Technology, Danvers, MA), 1:8000. Secondary anti-mouse IgG1 antibodies conjugated to Alexa Fluor 568, and anti-mouse IgG2a antibodies conjugated to Alexa Fluor 488 (Invitrogen), respectively, were diluted at 1:400, and DAPI was used at 1–10 µg/ml. Coverslips were mounted onto slides using ProLong Gold antifade and allowed to set hard in the dark at 4°C for at least 24 h, then sealed with clear nail polish before imaging.

Microscopy and image analysis

Epifluorescence microscopy was performed using an Olympus IX71 inverted microscope with 60× (1.40 NA) and 100× (1.35 NA) PlanApo objectives and a Coolsnap HQ camera (Photometrics, Tucson, AZ) or an Olympus IX71 inverted microscope with UPlanApo 100× (1.35 NA) or UPlanApo 60× (1.40 NA) objectives and Coolsnap ES^2 camera (Photometrics). Images were captured using Metamorph (Molecular Devices) or µManager software (Edelstein et al., 2010). Brightness/contrast levels were adjusted using ImageJ/Fiji version 2.0,0-rd-69/1.52p (Schneider et al., 2012) and Photoshop CS6 software (Adobe, San Jose, CA). For flagellar intensity measurements, ImageJ/Fiji was used to measure mean fluorescence intensity at 0.1-mm intervals along 53 individual mature flagella (i.e. data do not include new flagella) on methanol-fixed cells from three independent experiments. For flagellar length measurements, ImageJ/Fiji were used to measure lengths of PFR (stained with L8C4) in uninduced and induced methanol-fixed cells from four independent experiments.

Deconvolution microscopy was carried out using an Applied Precision DeltaVision Elite system (GE Healthcare Life Sciences, Pittsburgh, PA) with an Olympus IX71 inverted microscope with UPlanApo 100× (1.35 NA) or UPlanApo 60× (1.40 NA) objectives and Coolsnap ES^2 camera (Photometrics). Images were captured using Deltavision SoftWoRx v6 software (GE Healthcare). From 40–200 serial *z*-sections per channel were acquired at 0.10–0.40-µm intervals. Image *z*-stacks were deconvolved using SVI Huygens Professional v14 (Scientific Volume Imaging B.V., Hilversum, Netherlands) using Huygens' Classic Maximum Likelihood Estimation algorithm and experimental point source function (PSF) data generated by the UC Berkeley Biological Imaging Facility ('deconvolved *z*-stacks'). Images were analyzed using Bitplane Imaris v7 (Bitplane, Zurich, Switzerland) and ImageJ/Fiji. Two-dimensional maximum intensity projection images were generated from three-dimensional deconvolved stacks using Imaris, ImageJ/Fiji or Huygens Professional software. Image adjustments required for presentation were made using ImageJ/Fiji and Photoshop CS6.

For transmission electron microscopy (TEM), uninduced and induced RNAi cells were processed and thin sections generated as previously described (Tu et al., 2005), and were imaged using a JEOL 1200 transmission electron microscope.

Statistical analyses

Quantitative data were calculated and graphed using Excel (Microsoft Inc., Redmond, WA) and Prism 6 (GraphPad Software, La Jolla, CA). Sample sizes (n) were sufficient to detect statistical significance at the levels indicated. For colocalization analysis of IFT172 and IFT144 with TbKin2a (see Dunn et al., 2011), ImarisColoc (Bitplane, Zurich, Switzerland) was applied to deconvolved image *z*-stack data cropped to basal bodies-sized and single cell-sized blocks. For all such blocks, ImarisColoc was used to measure total threshold-adjusted signal colocalization for IFT172 and TbKin2a, or IFT144 and TbKin2a channel pairs. Threshold signal intensity lower cutoffs were determined per channel after evaluation of controls and relative sensitivities, and were generally set at 10% of maximum channel intensities. In Fig. 3F, final adjusted Mander's colocalization coefficient and adjusted Pearson's covariance coefficient statistics were computed and graphed using Prism 6. For Fig. 6A, the relative length statistics were computed using one-way analysis of variance (ANOVA) with Sidak's multiple comparison test with variance pooling, in Prism 6. Mean length differences between uninduced versus induced cell lines were significant at $P<0.0001$ using two-tailed tests. Mean length differences among uninduced cell lines, and between single knockdown induced cell lines, were all non-significant at $P<0.05$ using two tailed tests. For Fig. 6G, settling data statistics based on A_{600nm} absorption time point measurements were computed with Prism 6 using grouping analyses of uninduced versus induced cells by RNAi cell line using multiple *t*-tests, one two tailed *t*-test per cell line pair (induced versus uninduced) per time point (row), corrected for multiple comparisons using the Holm–Sidak method with 0.05 significance levels.

Acknowledgements

We dedicate this paper to the memory of Professor Ching C. Wang (1936-2017) of the University of California, San Francisco. We thank former members of the Wang lab – Ziyin Li, Xiaoming Tu, Stephane Gourguechon, and Praveen Kumar, among others – for reagents, procedures, unpublished observations, draft manuscript review (C.C.W. and Z.L.), insights, and encouragement. We thank Philippe Bastin, Benjamin Morga, and Thierry Blisnick of the Pasteur Institute for antibodies to IFT172 and IFT144, unpublished images, insights, and helpful suggestions. We thank Sam Dean at Oxford University for the generous gifts of pPOTv4 and pPOTv7 plasmids, as well as information, and advice. We thank Scott Dawson at UC Davis for insights and advice on phylogenetic methods and interpretation. We thank Ryan Case for insights and suggestions regarding bioinformatic analysis of kinesin motor domains and neck linkers. For reagents we thank: Keith Gull at Oxford University for antibodies (KMX, L8C4, L1B6, L3B2 and BBA4), Paul Englund at Johns Hopkins University for the pZJM vector, and George Cross at Rockefeller University for the 90-13 cell line. Denise Schichnes and Steve Ruzin of the UC Berkeley Biological Imaging Facility provided assistance with deconvolution microscopy, image processing, and analysis. Finally, we thank Welch lab members for their suggestions, support and patience.

Competing interests

The authors declare no competing or financial interests.

Author contributions

Conceptualization: R.L.D., B.M.H., A.A., M.D.W.; Methodology: R.L.D., B.M.H., A.A., H.W., R.L.J., J.M., W.Z.C., M.D.W.; Validation: R.L.D., B.M.H., A.A., H.W., R.L.J.; Formal analysis: R.L.D., B.M.H., A.A., H.W., M.D.W.; Investigation: R.L.D., B.M.H., A.A., H.W., R.L.J., J.M.; Data curation: R.L.D., B.M.H., A.A., H.W., W.Z.C., M.D.W.; Writing - original draft: R.L.D., M.D.W.; Writing - review & editing: R.L.D., B.M.H., A.A., H.W., R.L.J., J.M., W.Z.C., M.D.W.; Visualization: R.L.D., B.M.H., A.A., H.W., J.M.; Supervision: M.D.W.; Project administration: M.D.W.; Funding acquisition: R.L.D., M.D.W.

Funding

This work was funded in part by grant A40732 from the UNDP/World Bank/WHO Special Programme for Research and Training In Tropical Diseases (TDR). Funding was also provided by R.L.D., including through a family trust.

Supplementary information

Supplementary information available online at
https://jcs.biologists.org/lookup/doi/10.1242/jcs.129213.supplemental

References

Absalon, S., Blisnick, T., Kohl, L., Toutirais, G., Doré, G., Julkowska, D., Tavenet, A. and Bastin, P. (2008). Intraflagellar transport and functional analysis of genes required for flagellum formation in trypanosomes. *Mol. Biol. Cell* **19**, 929-944. doi:10.1091/mbc.e07-08-0749

Adhiambo, C., Blisnick, T., Toutirais, G., Delannoy, E. and Bastin, P. (2009). A novel function for the atypical small G protein Rab-like 5 in the assembly of the trypanosome flagellum. *J. Cell Sci.* **122**, 834-841. doi:10.1242/jcs.040444

Adl, S. M., Bass, D., Lane, C. E., Lukeš, J., Schoch, C. L., Smirnov, A., Agatha, S., Berney, C., Brown, M. W., Burki, F. et al. (2019). Revisions to the classification, nomenclature, and diversity of eukaryotes. *J. Eukaryot. Microbiol.* **66**, 4-119.

Akinsolu, F. T., Nemieboka, P. O., Njuguna, D. W., Ahadji, M. N., Dezso, D. and Varga, O. (2019). Emerging resistance of neglected tropical diseases: a scoping review of the literature. *Int. J. Environ. Res. Public Health* **16**, 1925. doi:10.3390/ijerph16111925

Bailey, T. L. and Elkan, C. (1994). Fitting a mixture model by expectation maximization to discover motifs in biopolymers. *Proc. Int. Conf. Intell. Syst. Mol. Biol.* **2**, 28-36.

Bailey, T. L. and Gribskov, M. (1998). Methods and statistics for combining motif match scores. *J. Comput. Biol.* **5**, 211-221. doi:10.1089/cmb.1998.5.211

Bailey, T. L., Williams, N., Misleh, C. and Li, W. W. (2006). MEME: discovering and analyzing DNA and protein sequence motifs. *Nucleic Acids Res.* **34**, W369-W373. doi:10.1093/nar/gkl198

Bailey, T. L., Boden, M., Buske, F. A., Frith, M., Grant, C. E., Clementi, L., Ren, J., Li, W. W. and Noble, W. S. (2009). MEME SUITE: tools for motif discovery and searching. *Nucleic Acids Res.* **37**, W202-W208. doi:10.1093/nar/gkp335

Bastin, P., Pullen, T. J., Sherwin, T. and Gull, K. (1999). Protein transport and flagellum assembly dynamics revealed by analysis of the paralysed trypanosome mutant snl-1. *J. Cell Sci.* **112**, 3769-3777.

Berriman, M., Ghedin, E., Hertz-Fowler, C., Blandin, G., Renauld, H., Bartholomeu, D. C., Lennard, N. J., Caler, E., Hamlin, N. E., Haas, B. et al. (2005). The genome of the African trypanosome Trypanosoma brucei. *Science* **309**, 416-422. doi:10.1126/science.1112642

Bertiaux, E., Morga, B., Blisnick, T., Rotureau, B. and Bastin, P. (2018a). A grow-and-lock model for the control of flagellum length in trypanosomes. *Curr. Biol.* **28**, 3802-3814.e3. doi:10.1016/j.cub.2018.10.031

Bertiaux, E., Mallet, A., Fort, C., Blisnick, T., Bonnefoy, S., Jung, J., Lemos, M., Marco, S., Vaughan, S., Trépout, S. et al. (2018b). Bidirectional intraflagellar

transport is restricted to two sets of microtubule doublets in the trypanosome flagellum. *J. Cell Biol.* **217**, 4284-4297. doi:10.1083/jcb.201805030

Bhogaraju, S., Cajanek, L., Fort, C., Blisnick, T., Weber, K., Taschner, M., Mizuno, N., Lamla, S., Bastin, P., Nigg, E. A. et al. (2013). Molecular basis of tubulin transport within the cilium by IFT74 and IFT81. *Science* **341**, 1009-1012. doi:10.1126/science.1240985

Birkett, C. R., Foster, K. E., Johnson, L. and Gull, K. (1985). Use of monoclonal antibodies to analyse the expression of a multi-tubulin family. *FEBS Lett.* **187**, 211-218. doi:10.1016/0014-5793(85)81244-8

Blaineau, C., Tessier, M., Dubessay, P., Tasse, L., Crobu, L., Pagès, M. and Bastien, P. (2007). A novel microtubule-depolymerizing kinesin involved in length control of a eukaryotic flagellum. *Curr. Biol.* **17**, 778-782. doi:10.1016/j.cub.2007.03.048

Blisnick, T., Buisson, J., Absalon, S., Marie, A., Cayet, N. and Bastin, P. (2014). The intraflagellar transport dynein complex of trypanosomes is made of a heterodimer of dynein heavy chains and of light and intermediate chains of distinct functions. *Mol. Biol. Cell* **25**, 2620-2633. doi:10.1091/mbc.e14-05-0961

Blum, T., Briesemeister, S. and Kohlbacher, O. (2009). MultiLoc2: integrating phylogeny and Gene Ontology terms improves subcellular protein localization prediction. *BMC Bioinformatics* **10**, 274. doi:10.1186/1471-2105-10-274

Brameier, M., Krings, A. and MacCallum, R. M. (2007). NucPred–predicting nuclear localization of proteins. *Bioinformatics* **23**, 1159-1160. doi:10.1093/bioinformatics/btm066

Brenndörfer, M. and Boshart, M. (2010). Selection of reference genes for mRNA quantification in Trypanosoma brucei. *Mol. Biochem. Parasitol.* **172**, 52-55. doi:10.1016/j.molbiopara.2010.03.007

Broadhead, R., Dawe, H. R., Farr, H., Griffiths, S., Hart, S. R., Portman, N., Shaw, M. K., Ginger, M. L., Gaskell, S. J., McKean, P. G. et al. (2006). Flagellar motility is required for the viability of the bloodstream trypanosome. *Nature* **440**, 224-227. doi:10.1038/nature04541

Brown, J. M., Marsala, C., Kosoy, R. and Gaertig, J. (1999). Kinesin-II is preferentially targeted to assembling cilia and is required for ciliogenesis and normal cytokinesis in Tetrahymena. *Mol. Biol. Cell* **10**, 3081-3096. doi:10.1091/mbc.10.10.3081

Brown, A. K., Hunt, S. D. and Stephens, D. J. (2014). Opposing microtubule motors control motility, morphology and cargo segregation during ER-to-Golgi transport. *Biol. Open* **3**, 307-313. doi:10.1242/bio.20147633

Buisson, J., Chenouard, N., Lagache, T., Blisnick, T., Olivo-Marin, J.-C. and Bastin, P. (2013). Intraflagellar transport proteins cycle between the flagellum and its base. *J. Cell Sci.* **126**, 327-338. doi:10.1242/jcs.117069

Burkard, G., Fragoso, C. M. and Roditi, I. (2007). Highly efficient stable transformation of bloodstream forms of Trypanosoma brucei. *Mol. Biochem. Parasitol.* **153**, 220-223. doi:10.1016/j.molbiopara.2007.02.008

Büscher, P., Cecchi, G., Jamonneau, V. and Priotto, G. (2017). Human African trypanosomiasis. *Lancet* **390**, 2397-2409. doi:10.1016/S0140-6736(17)31510-6

Carruthers, V. B. and Cross, G. A. (1992). High-efficiency clonal growth of bloodstream- and insect-form Trypanosoma brucei on agarose plates. *Proc. Natl. Acad. Sci. USA* **89**, 8818-8821. doi:10.1073/pnas.89.18.8818

Case, R. B., Rice, S., Hart, C. L., Ly, B. and Vale, R. D. (2000). Role of the kinesin neck linker and catalytic core in microtubule-based motility. *Curr. Biol.* **10**, 157-160. doi:10.1016/S0960-9822(00)00316-X

Cayla, M., Rojas, F., Silvester, E., Venter, F. and Matthews, K. R. (2019). African trypanosomes. *Parasit. Vectors* **12**, 190. doi:10.1186/s13071-019-3355-5

Chan, K. Y. and Ersfeld, K. (2010). The role of the Kinesin-13 family protein TbKif13-2 in flagellar length control of Trypanosoma brucei. *Mol. Biochem. Parasitol.* **174**, 137-140. doi:10.1016/j.molbiopara.2010.08.001

Cole, D. G., Chinn, S. W., Wedaman, K. P., Hall, K., Vuong, T. and Scholey, J. M. (1993). Novel heterotrimeric kinesin-related protein purified from sea urchin eggs. *Nature* **366**, 268-270. doi:10.1038/366268a0

Cole, D. G., Diener, D. R., Himelblau, A. L., Beech, P. L., Fuster, J. C. and Rosenbaum, J. L. (1998). Chlamydomonas kinesin-II-dependent intraflagellar transport (IFT): IFT particles contain proteins required for ciliary assembly in Caenorhabditis elegans sensory neurons. *J. Cell Biol.* **141**, 993-1008. doi:10.1083/jcb.141.4.993

de Graffenried, C. L., Ho, H. H. and Warren, G. (2008). Polo-like kinase is required for Golgi and bilobe biogenesis in Trypanosoma brucei. *J. Cell Biol.* **181**, 431-438. doi:10.1083/jcb.200708082

de Graffenried, C. L., Anrather, D., Von Raußendorf, F. and Warren, G. (2013). Polo-like kinase phosphorylation of bilobe-resident TbCentrin2 facilitates flagellar inheritance in Trypanosoma brucei. *Mol. Biol. Cell* **24**, 1947-1963. doi:10.1091/mbc.e12-12-0911

De Marco, V., Burkhard, P., Le Bot, N., Vernos, I. and Hoenger, A. (2001). Analysis of heterodimer formation by Xklp3A/B, a newly cloned kinesin-II from Xenopus laevis. *EMBO J.* **20**, 3370-3379. doi:10.1093/emboj/20.13.3370

De Marco, V., De Marco, A., Goldie, K. N., Correia, J. J. and Hoenger, A. (2003). Dimerization properties of a Xenopus laevis kinesin-II carboxy-terminal stalk fragment. *EMBO Rep.* **4**, 717-722. doi:10.1038/sj.embor.embor884

Dean, S., Sunter, J., Wheeler, R. J., Hodkinson, I., Gluenz, E. and Gull, K. (2015). A toolkit enabling efficient, scalable and reproducible gene tagging in trypanosomatids. *Open Biol.* **5**, 140197. doi:10.1098/rsob.140197

Deane, J. A., Cole, D. G., Seeley, E. S., Diener, D. R. and Rosenbaum, J. L. (2001). Localization of intraflagellar transport protein IFT52 identifies basal body transitional fibers as the docking site for IFT particles. *Curr. Biol.* **11**, 1586-1590. doi:10.1016/S0960-9822(01)00484-5

Demonchy, R., Blisnick, T., Deprez, C., Toutirais, G., Loussert, C., Marande, W., Grellier, P., Bastin, P. and Kohl, L. (2009). Kinesin 9 family members perform separate functions in the trypanosome flagellum. *J. Cell Biol.* **187**, 615-622. doi:10.1083/jcb.200903139

Dishinger, J. F., Kee, H. L., Jenkins, P. M., Fan, S., Hurd, T. W., Hammond, J. W., Truong, Y. N.-T., Margolis, B., Martens, J. R. and Verhey, K. J. (2010). Ciliary entry of the kinesin-2 motor KIF17 is regulated by importin-β2 and RanGTP. *Nat. Cell Biol.* **12**, 703-710. doi:10.1038/ncb2073

Doodhi, H., Ghosal, D., Krishnamurthy, M., Jana, S. C., Shamala, D., Bhaduri, A., Sowdhamini, R. and Ray, K. (2009). KAP, the accessory subunit of kinesin-2, binds the predicted coiled-coil stalk of the motor subunits. *Biochemistry* **48**, 2248-2260. doi:10.1021/bi8018338

Dunn, K. W., Kamocka, M. M. and McDonald, J. H. (2011). A practical guide to evaluating colocalization in biological microscopy. *Am. J. Physiol. Cell Physiol.* **300**, C723-C742. doi:10.1152/ajpcell.00462.2010

Durand-Dubief, M. and Bastin, P. (2003). TbAGO1, an argonaute protein required for RNA interference, is involved in mitosis and chromosome segregation in Trypanosoma brucei. *BMC Biol.* **1**, 2. doi:10.1186/1741-7007-1-2

Edelstein, A., Amodaj, N., Hoover, K., Vale, R. and Stuurman, N. (2010). Computer control of microscopes using μManager. *Curr. Protoc. Mol. Biol.* Chapter 14, Unit 14.20. doi:10.1002/0471142727.mb1420s92

Engstler, M., Pfohl, T., Herminghaus, S., Boshart, M., Wiegertjes, G., Heddergott, N. and Overath, P. (2007). Hydrodynamic flow-mediated protein sorting on the cell surface of trypanosomes. *Cell* **131**, 505-515. doi:10.1016/j.cell.2007.08.046

Evan, G. I., Lewis, G. K., Ramsay, G. and Bishop, J. M. (1985). Isolation of monoclonal antibodies specific for human c-myc proto-oncogene product. *Mol. Cell. Biol.* **5**, 3610-3616. doi:10.1128/MCB.5.12.3610

Fairlamb, A. H. and Horn, D. (2018). Melarsoprol resistance in African Trypanosomiasis. *Trends Parasitol.* **34**, 481-492. doi:10.1016/j.pt.2018.04.002

Fan, J. and Beck, K. A. (2004). A role for the spectrin superfamily member Syne-1 and kinesin II in cytokinesis. *J. Cell Sci.* **117**, 619-629. doi:10.1242/jcs.00892

Farr, H. and Gull, K. (2009). Functional studies of an evolutionarily conserved, cytochrome b5 domain protein reveal a specific role in axonemal organisation and the general phenomenon of post-division axonemal growth in trypanosomes. *Cell Motil. Cytoskeleton* **66**, 24-35. doi:10.1002/cm.20322

Farr, H. and Gull, K. (2012). Cytokinesis in trypanosomes. *Cytoskeleton (Hoboken)* **69**, 931-941. doi:10.1002/cm.21074

Field, M. C., Horn, D., Fairlamb, A. H., Ferguson, M. A. J., Gray, D. W., Read, K. D., De Rycker, M., Torrie, L. S., Wyatt, P. G., Wyllie, S. et al. (2017). Anti-trypanosomatid drug discovery: an ongoing challenge and a continuing need. *Nat. Rev. Microbiol.* **15**, 217-231. doi:10.1038/nrmicro.2016.193

Fort, C., Bonnefoy, S., Kohl, L. and Bastin, P. (2016). Intraflagellar transport is required for the maintenance of the trypanosome flagellum composition but not its length. *J. Cell Sci.* **129**, 3026-3041. doi:10.1242/jcs.188227

Franklin, J. B. and Ullu, E. (2010). Biochemical analysis of PIFTC3, the Trypanosoma brucei orthologue of nematode DYF-13, reveals interactions with established and putative intraflagellar transport components. *Mol. Microbiol.* **78**, 173-186. doi:10.1111/j.1365-2958.2010.07322.x

Gadelha, C., Rothery, S., Morphew, M., McIntosh, J. R., Severs, N. J. and Gull, K. (2009). Membrane domains and flagellar pocket boundaries are influenced by the cytoskeleton in African trypanosomes. *Proc. Natl. Acad. Sci. USA* **106**, 17425-17430. doi:10.1073/pnas.0909289106

Gheiratmand, L., Brasseur, A., Zhou, Q. and He, C. Y. (2013). Biochemical characterization of the bi-lobe reveals a continuous structural network linking the bi-lobe to other single-copied organelles in Trypanosoma brucei. *J. Biol. Chem.* **288**, 3489-3499. doi:10.1074/jbc.M112.417428

Gluenz, E., Povelones, M. L., Englund, P. T. and Gull, K. (2011). The kinetoplast duplication cycle in Trypanosoma brucei is orchestrated by cytoskeleton-mediated cell morphogenesis. *Mol. Cell. Biol.* **31**, 1012-1021. doi:10.1128/MCB.01176-10

Goetz, S. C. and Anderson, K. V. (2010). The primary cilium: a signalling centre during vertebrate development. *Nat. Rev. Genet.* **11**, 331-344. doi:10.1038/nrg2774

Goodson, H. V., Kang, S. J. and Endow, S. A. (1994). Molecular phylogeny of the kinesin family of microtubule motor proteins. *J. Cell Sci.* **107**, 1875-1884.

Granger, E., McNee, G., Allan, V. and Woodman, P. (2014). The role of the cytoskeleton and molecular motors in endosomal dynamics. *Semin. Cell Dev. Biol.* **31**, 20-29. doi:10.1016/j.semcdb.2014.04.011

Gull, K. (1999). The cytoskeleton of trypanosomatid parasites. *Annu. Rev. Microbiol.* **53**, 629-655. doi:10.1146/annurev.micro.53.1.629

Hammarton, T. C., Kramer, S., Tetley, L., Boshart, M. and Mottram, J. C. (2007a). Trypanosoma brucei Polo-like kinase is essential for basal body duplication, kDNA segregation and cytokinesis. *Mol. Microbiol.* **65**, 1229-1248. doi:10.1111/j.1365-2958.2007.05866.x

Hammarton, T. C., Monnerat, S. and Mottram, J. C. (2007b). Cytokinesis in trypanosomatids. *Curr. Opin. Microbiol.* **10**, 520-527. doi:10.1016/j.mib.2007.10.005
Haraguchi, K., Hayashi, T., Jimbo, T., Yamamoto, T. and Akiyama, T. (2006). Role of the kinesin-2 family protein, KIF3, during mitosis. *J. Biol. Chem.* **281**, 4094-4099. doi:10.1074/jbc.M507028200
Heddergott, N., Krüger, T., Babu, S. B., Wei, A., Stellamanns, E., Uppaluri, S., Pfohl, T., Stark, H. and Engstler, M. (2012). Trypanosome motion represents an adaptation to the crowded environment of the vertebrate bloodstream. *PLoS Pathog.* **8**, e1003023. doi:10.1371/journal.ppat.1003023
Hesse, F., Selzer, P. M., Mühlstädt, K. and Duszenko, M. (1995). A novel cultivation technique for long-term maintenance of bloodstream form trypanosomes in vitro. *Mol. Biochem. Parasitol.* **70**, 157-166. doi:10.1016/0166-6851(95)00027-X
Hilton, N. A., Sladewski, T. E., Perry, J. A., Pataki, Z., Sinclair-Davis, A. N., Muniz, R. S., Tran, H. L., Wurster, J. I., Seo, J. and de Graffenried, C. L. (2018). Identification of TOEFAZ1-interacting proteins reveals key regulators of Trypanosoma brucei cytokinesis. *Mol. Microbiol.* **109**, 306-326. doi:10.1111/mmi.13986
Hirokawa, N., Niwa, S. and Tanaka, Y. (2010). Molecular motors in neurons: transport mechanisms and roles in brain function, development, and disease. *Neuron* **68**, 610-638. doi:10.1016/j.neuron.2010.09.039
Hoffmann, A., Käser, S., Jakob, M., Amodeo, S., Peitsch, C., Týč, J., Vaughan, S., Zuber, B., Schneider, A. and Ochsenreiter, T. (2018). Molecular model of the mitochondrial genome segregation machinery in Trypanosoma brucei. *Proc. Natl. Acad. Sci. USA* **115**, E1809-E1818. doi:10.1073/pnas.1716582115
Höög, J. L., Bouchet-Marquis, C., McIntosh, J. R., Hoenger, A. and Gull, K. (2012). Cryo-electron tomography and 3-D analysis of the intact flagellum in Trypanosoma brucei. *J. Struct. Biol.* **178**, 189-198. doi:10.1016/j.jsb.2012.01.009
Huet, D., Blisnick, T., Perrot, S. and Bastin, P. (2014). The GTPase IFT27 is involved in both anterograde and retrograde intraflagellar transport. *eLife* **3**, e02419. doi:10.7554/eLife.02419
Huet, D., Blisnick, T., Perrot, S. and Bastin, P. (2019). IFT25 is required for the construction of the trypanosome flagellum. *J. Cell. Sci.* **132**, jcs228296. doi:10.1242/jcs.228296
Hughes, L., Towers, K., Starborg, T., Gull, K. and Vaughan, S. (2013). A cell-body groove housing the new flagellum tip suggests an adaptation of cellular morphogenesis for parasitism in the bloodstream form of Trypanosoma brucei. *J. Cell. Sci.* **126**, 5748-5757. doi:10.1242/jcs.139139
Ikeda, K. N. and de Graffenried, C. L. (2012). Polo-like kinase is necessary for flagellum inheritance in Trypanosoma brucei. *J. Cell Sci.* **125**, 3173-3184. doi:10.1242/jcs.101162
Imanishi, M., Endres, N. F., Gennerich, A. and Vale, R. D. (2006). Autoinhibition regulates the motility of the C. elegans intraflagellar transport motor OSM-3. *J. Cell Biol.* **174**, 931-937. doi:10.1083/jcb.200605179
Insinna, C. and Besharse, J. C. (2008). Intraflagellar transport and the sensory outer segment of vertebrate photoreceptors. *Dev. Dyn.* **237**, 1982-1992. doi:10.1002/dvdy.21554
Ishikawa, H. and Marshall, W. F. (2011). Ciliogenesis: building the cell's antenna. *Nat. Rev. Mol. Cell Biol.* **12**, 222-234. doi:10.1038/nrm3085
Julkowska, D. and Bastin, P. (2009). Tools for analyzing intraflagellar transport in trypanosomes. *Methods Cell Biol.* **93**, 59-80. doi:10.1016/S0091-679X(08)93003-X
Kee, H. L., Dishinger, J. F., Blasius, T. L., Liu, C.-J., Margolis, B. and Verhey, K. J. (2012). A size-exclusion permeability barrier and nucleoporins characterize a ciliary pore complex that regulates transport into cilia. *Nat. Cell Biol.* **14**, 431-437. doi:10.1038/ncb2450
Kennedy, P. G. E. (2019). Update on human African trypanosomiasis (sleeping sickness). *J. Neurol.* **266**, 2334-2337. doi:10.1007/s00415-019-09425-7
Kennedy, P. G. E. and Rodgers, J. (2019). Clinical and neuropathogenetic aspects of human African trypanosomiasis. *Front. Immunol.* **10**, 39. doi:10.3389/fimmu.2019.00039
Kisalu, N. K., Langousis, G., Bentolila, L. A., Ralston, K. S. and Hill, K. L. (2014). Mouse infection and pathogenesis by Trypanosoma brucei motility mutants. *Cell. Microbiol.* **16**, 912-924. doi:10.1111/cmi.12244
Kohl, L. and Bastin, P. (2005). The flagellum of trypanosomes. *Int. Rev. Cytol.* **244**, 227-285. doi:10.1016/S0074-7696(05)44006-1
Kohl, L., Sherwin, T. and Gull, K. (1999). Assembly of the paraflagellar rod and the flagellum attachment zone complex during the Trypanosoma brucei cell cycle. *J. Eukaryot. Microbiol.* **46**, 105-109. doi:10.1111/j.1550-7408.1999.tb04592.x
Kohl, L., Robinson, D. and Bastin, P. (2003). Novel roles for the flagellum in cell morphogenesis and cytokinesis of trypanosomes. *EMBO J.* **22**, 5336-5346. doi:10.1093/emboj/cdg518
Kozminski, K. G., Johnson, K. A., Forscher, P. and Rosenbaum, J. L. (1993). A motility in the eukaryotic flagellum unrelated to flagellar beating. *Proc. Natl. Acad. Sci. USA* **90**, 5519-5523. doi:10.1073/pnas.90.12.5519
Kozminski, K. G., Beech, P. L. and Rosenbaum, J. L. (1995). The Chlamydomonas kinesin-like protein FLA10 is involved in motility associated with the flagellar membrane. *J. Cell Biol.* **131**, 1517-1527. doi:10.1083/jcb.131.6.1517
Krüger, T., Schuster, S. and Engstler, M. (2018). Beyond blood: African trypanosomes on the move. *Trends Parasitol.* **34**, 1056-1067. doi:10.1016/j.pt.2018.08.002
Kumar, P. and Wang, C. C. (2006). Dissociation of cytokinesis initiation from mitotic control in a eukaryote. *Eukaryot. Cell* **5**, 92-102. doi:10.1128/EC.5.1.92-102.2006
Lacomble, S., Vaughan, S., Gadelha, C., Morphew, M. K., Shaw, M. K., McIntosh, J. R. and Gull, K. (2009). Three-dimensional cellular architecture of the flagellar pocket and associated cytoskeleton in trypanosomes revealed by electron microscope tomography. *J. Cell Sci.* **122**, 1081-1090. doi:10.1242/jcs.045740
Lacomble, S., Vaughan, S., Gadelha, C., Morphew, M. K., Shaw, M. K., McIntosh, J. R. and Gull, K. (2010). Basal body movements orchestrate membrane organelle division and cell morphogenesis in Trypanosoma brucei. *J. Cell Sci.* **123**, 2884-2891. doi:10.1242/jcs.074161
LaCount, D. J., Barrett, B. and Donelson, J. E. (2002). Trypanosoma brucei FLA1 is required for flagellum attachment and cytokinesis. *J. Biol. Chem.* **277**, 17580-17588. doi:10.1074/jbc.M200873200
Langousis, G. and Hill, K. L. (2014). Motility and more: the flagellum of Trypanosoma brucei. *Nat. Rev. Microbiol.* **12**, 505-518. doi:10.1038/nrmicro3274
Lechtreck, K. F. (2015). IFT-cargo interactions and protein transport in Cilia. *Trends Biochem. Sci.* **40**, 765-778. doi:10.1016/j.tibs.2015.09.003
Li, Z. and Wang, C. C. (2006). Changing roles of aurora-B kinase in two life cycle stages of Trypanosoma brucei. *Eukaryot. Cell* **5**, 1026-1035. doi:10.1128/EC.00129-06
Li, Z., Umeyama, T., Li, Z. and Wang, C. C. (2010). Polo-like kinase guides cytokinesis in Trypanosoma brucei through an indirect means. *Eukaryot. Cell* **9**, 705-716. doi:10.1128/EC.00330-09
Marande, W. and Kohl, L. (2011). Flagellar kinesins in protists. *Future Microbiol.* **6**, 231-246. doi:10.2217/fmb.10.167
Mesu, V. K. B. K., Kalonji, W. M., Bardonneau, C., Mordt, O. V., Blesson, S., Simon, F., Delhomme, S., Bernhard, S., Kuziena, W., Lubaki, J.-P. F. et al. (2018). Oral fexinidazole for late-stage African Trypanosoma brucei gambiense trypanosomiasis: a pivotal multicentre, randomised, non-inferiority trial. *Lancet* **391**, 144-154. doi:10.1016/S0140-6736(17)32758-7
Miller, M. S., Esparza, J. M., Lippa, A. M., Lux, F. G., Cole, D. G. and Dutcher, S. K. (2005). Mutant kinesin-2 motor subunits increase chromosome loss. *Mol. Biol. Cell* **16**, 3810-3820. doi:10.1091/mbc.e05-05-0404
Mogk, S., Boßelmann, C. M., Mudogo, C. N., Stein, J., Wolburg, H. and Duszenko, M. (2017). African trypanosomes and brain infection - the unsolved question. *Biol. Rev. Camb. Philos. Soc.* **92**, 1675-1687. doi:10.1111/brv.12301
Morris, J. C., Wang, Z., Drew, M. E., Paul, K. S. and Englund, P. T. (2001). Inhibition of bloodstream form Trypanosoma brucei gene expression by RNA interference using the pZJM dual T7 vector. *Mol. Biochem. Parasitol.* **117**, 111-113. doi:10.1016/S0166-6851(01)00334-6
Mueller, J., Perrone, C. A., Bower, R., Cole, D. G. and Porter, M. E. (2005). The FLA3 KAP subunit is required for localization of kinesin-2 to the site of flagellar assembly and processive anterograde intraflagellar transport. *Mol. Biol. Cell* **16**, 1341-1354. doi:10.1091/mbc.e04-10-0931
Oberholzer, M., Langousis, G., Nguyen, H. K. T., Saada, E. A., Shimogawa, M. M., Jonsson, Z. O., Nguyen, S. M., Wohlschlegel, J. A. and Hill, K. L. (2011). Independent analysis of the flagellum surface and matrix proteomes provides insight into flagellum signaling in mammalian-infectious Trypanosoma brucei. *Mol. Cell Proteomics* **10**, M111.010538. doi:10.1074/mcp.M111.010538
Ogbadoyi, E. O., Robinson, D. R. and Gull, K. (2003). A high-order trans-membrane structural linkage is responsible for mitochondrial genome positioning and segregation by flagellar basal bodies in trypanosomes. *Mol. Biol. Cell* **14**, 1769-1779. doi:10.1091/mbc.e02-08-0525
Pigino, G., Geimer, S., Lanzavecchia, S., Paccagnini, E., Cantele, F., Diener, D. R., Rosenbaum, J. L. and Lupetti, P. (2009). Electron-tomographic analysis of intraflagellar transport particle trains in situ. *J. Cell Biol.* **187**, 135-148. doi:10.1083/jcb.200905103
Piperno, G. and Mead, K. (1997). Transport of a novel complex in the cytoplasmic matrix of Chlamydomonas flagella. *Proc. Natl. Acad. Sci. USA* **94**, 4457-4462. doi:10.1073/pnas.94.9.4457
Piperno, G., Mead, K. and Henderson, S. (1996). Inner dynein arms but not outer dynein arms require the activity of kinesin homologue protein KHP1(FLA10) to reach the distal part of flagella in Chlamydomonas. *J. Cell Biol.* **133**, 371-379. doi:10.1083/jcb.133.2.371
Prevo, B., Mangeol, P., Oswald, F., Scholey, J. M. and Peterman, E. J. G. (2015). Functional differentiation of cooperating kinesin-2 motors orchestrates cargo import and transport in C. elegans cilia. *Nat. Cell Biol.* **17**, 1536-1545. doi:10.1038/ncb3263
Prevo, B., Scholey, J. M. and Peterman, E. J. G. (2017). Intraflagellar transport: mechanisms of motor action, cooperation, and cargo delivery. *FEBS J.* **284**, 2905-2931. doi:10.1111/febs.14068
Ralston, K. S. and Hill, K. L. (2006). Trypanin, a component of the flagellar Dynein regulatory complex, is essential in bloodstream form African trypanosomes. *PLoS Pathog.* **2**, e101. doi:10.1371/journal.ppat.0020101
Ralston, K. S., Lerner, A. G., Diener, D. R. and Hill, K. L. (2006). Flagellar motility contributes to cytokinesis in Trypanosoma brucei and is modulated by an evolutionarily conserved dynein regulatory system. *Eukaryot. Cell* **5**, 696-711. doi:10.1128/EC.5.4.696-711.2006

Ralston, K. S., Kabututu, Z. P., Melehani, J. H., Oberholzer, M. and Hill, K. L. (2009). The Trypanosoma brucei flagellum: moving parasites in new directions. *Annu. Rev. Microbiol.* **63**, 335-362. doi:10.1146/annurev.micro.091208.073353
Ralston, K. S., Kisalu, N. K. and Hill, K. L. (2011). Structure-function analysis of dynein light chain 1 identifies viable motility mutants in bloodstream-form Trypanosoma brucei. *Eukaryot. Cell* **10**, 884-894. doi:10.1128/EC.00298-10
Redmond, S., Vadivelu, J. and Field, M. C. (2003). RNAit: an automated web-based tool for the selection of RNAi targets in Trypanosoma brucei. *Mol. Biochem. Parasitol.* **128**, 115-118. doi:10.1016/S0166-6851(03)00045-8
Robinson, D. R. and Gull, K. (1991). Basal body movements as a mechanism for mitochondrial genome segregation in the trypanosome cell cycle. *Nature* **352**, 731-733. doi:10.1038/352731a0
Robinson, D., Beattie, P., Sherwin, T. and Gull, K. (1991). Microtubules, tubulin, and microtubule-associated proteins of trypanosomes. *Meth. Enzymol.* **196**, 285-299. doi:10.1016/0076-6879(91)96027-O
Robinson, D. R., Sherwin, T., Ploubidou, A., Byard, E. H. and Gull, K. (1995). Microtubule polarity and dynamics in the control of organelle positioning, segregation, and cytokinesis in the trypanosome cell cycle. *J. Cell Biol.* **128**, 1163-1172. doi:10.1083/jcb.128.6.1163
Rodríguez, J. A., Lopez, M. A., Thayer, M. C., Zhao, Y., Oberholzer, M., Chang, D. D., Kisalu, N. K., Penichet, M. L., Helguera, G., Bruinsma, R. et al. (2009). Propulsion of African trypanosomes is driven by bihelical waves with alternating chirality separated by kinks. *Proc. Natl. Acad. Sci. USA* **106**, 19322-19327. doi:10.1073/pnas.0907001106
Sagolla, M. S., Dawson, S. C., Mancuso, J. J. and Cande, W. Z. (2006). Three-dimensional analysis of mitosis and cytokinesis in the binucleate parasite Giardia intestinalis. *J. Cell Sci.* **119**, 4889-4900. doi:10.1242/jcs.03276
Schmittgen, T. D. and Livak, K. J. (2008). Analyzing real-time PCR data by the comparative C(T) method. *Nat. Protoc.* **3**, 1101-1108. doi:10.1038/nprot.2008.73
Schneider, A. and Ochsenreiter, T. (2018). Failure is not an option - mitochondrial genome segregation in trypanosomes. *J. Cell. Sci.* **131**, jcs221820. doi:10.1242/jcs.221820
Schneider, C. A., Rasband, W. S. and Eliceiri, K. W. (2012). NIH Image to ImageJ: 25 years of image analysis. *Nat. Methods* **9**, 671-675. doi:10.1038/nmeth.2089
Scholey, J. M. (2013). Kinesin-2: a family of heterotrimeric and homodimeric motors with diverse intracellular transport functions. *Annu. Rev. Cell Dev. Biol.* **29**, 443-469. doi:10.1146/annurev-cellbio-101512-122335
Schroeder, A., Mueller, O., Stocker, S., Salowsky, R., Leiber, M., Gassmann, M., Lightfoot, S., Menzel, W., Granzow, M. and Ragg, T. (2006). The RIN: an RNA integrity number for assigning integrity values to RNA measurements. *BMC Mol. Biol.* **7**, 3. doi:10.1186/1471-2199-7-3
Schumann Burkard, G., Jutzi, P. and Roditi, I. (2011). Genome-wide RNAi screens in bloodstream form trypanosomes identify drug transporters. *Mol. Biochem. Parasitol.* **175**, 91-94. doi:10.1016/j.molbiopara.2010.09.002
Selvapandiyan, A., Kumar, P., Morris, J. C., Salisbury, J. L., Wang, C. C. and Nakhasi, H. L. (2007). Centrin1 is required for organelle segregation and cytokinesis in Trypanosoma brucei. *Mol. Biol. Cell* **18**, 3290-3301. doi:10.1091/mbc.e07-01-0022
Sherwin, T. and Gull, K. (1989). The cell division cycle of Trypanosoma brucei brucei: timing of event markers and cytoskeletal modulations. *Philos. Trans. R. Soc. Lond. B Biol. Sci.* **323**, 573-588. doi:10.1098/rstb.1989.0037
Shi, J., Franklin, J. B., Yelinek, J. T., Ebersberger, I., Warren, G. and He, C. Y. (2008). Centrin4 coordinates cell and nuclear division in T. brucei. *J. Cell Sci.* **121**, 3062-3070. doi:10.1242/jcs.030643
Shimogawa, M. M., Ray, S. S., Kisalu, N., Zhang, Y., Geng, Q., Ozcan, A. and Hill, K. L. (2018). Parasite motility is critical for virulence of African trypanosomes. *Sci. Rep.* **8**, 9122. doi:10.1038/s41598-018-27228-0
Signor, D., Wedaman, K. P., Rose, L. S. and Scholey, J. M. (1999). Two heteromeric kinesin complexes in chemosensory neurons and sensory cilia of Caenorhabditis elegans. *Mol. Biol. Cell* **10**, 345-360. doi:10.1091/mbc.10.2.345
Sinclair-Davis, A. N., McAllaster, M. R. and de Graffenried, C. L. (2017). A functional analysis of TOEFAZ1 uncovers protein domains essential for cytokinesis in Trypanosoma brucei. *J. Cell. Sci.* **130**, 3918-3932. doi:10.1242/jcs.207209
Snow, J. J., Ou, G., Gunnarson, A. L., Walker, M. R. S., Zhou, H. M., Brust-Mascher, I. and Scholey, J. M. (2004). Two anterograde intraflagellar transport motors cooperate to build sensory cilia on C. elegans neurons. *Nat. Cell Biol.* **6**, 1109-1113. doi:10.1038/ncb1186
Stauber, T., Simpson, J. C., Pepperkok, R. and Vernos, I. (2006). A role for kinesin-2 in COPI-dependent recycling between the ER and the Golgi complex. *Curr. Biol.* **16**, 2245-2251. doi:10.1016/j.cub.2006.09.060
Sun, L. and Wang, C. C. (2011). The structural basis of localizing polo-like kinase to the flagellum attachment zone in Trypanosoma brucei. *PLoS ONE* **6**, e27303. doi:10.1371/journal.pone.0027303
Sunter, J. D. and Gull, K. (2016). The flagellum attachment zone: 'The Cellular Ruler' of trypanosome morphology. *Trends Parasitol.* **32**, 309-324. doi:10.1016/j.pt.2015.12.010
Sunter, J. D., Varga, V., Dean, S. and Gull, K. (2015). A dynamic coordination of flagellum and cytoplasmic cytoskeleton assembly specifies cell morphogenesis in trypanosomes. *J. Cell Sci.* **128**, 1580-1594. doi:10.1242/jcs.166447
Tan, K. S. W., Leal, S. T. G. and Cross, G. A. M. (2002). Trypanosoma brucei MRE11 is non-essential but influences growth, homologous recombination and DNA double-strand break repair. *Mol. Biochem. Parasitol.* **125**, 11-21. doi:10.1016/S0166-6851(02)00165-2
Taschner, M. and Lorentzen, E. (2016). The intraflagellar transport machinery. *Cold Spring Harb. Perspect. Biol.* **8**, a028092. doi:10.1101/cshperspect.a028092
Taylor, A. E. and Godfrey, D. G. (1969). A new organelle of bloodstream salivarian trypanosomes. *J. Protozool.* **16**, 466-470. doi:10.1111/j.1550-7408.1969.tb02302.x
Tu, X. and Wang, C. C. (2004). The involvement of two cdc2-related kinases (CRKs) in Trypanosoma brucei cell cycle regulation and the distinctive stage-specific phenotypes caused by CRK3 depletion. *J. Biol. Chem.* **279**, 20519-20528. doi:10.1074/jbc.M312862200
Tu, X., Mancuso, J., Cande, W. Z. and Wang, C. C. (2005). Distinct cytoskeletal modulation and regulation of G1-S transition in the two life stages of Trypanosoma brucei. *J. Cell Sci.* **118**, 4353-4364. doi:10.1242/jcs.02567
Umeyama, T. and Wang, C. C. (2008). Polo-like kinase is expressed in S/G2/M phase and associated with the flagellum attachment zone in both procyclic and bloodstream forms of Trypanosoma brucei. *Eukaryot. Cell* **7**, 1582-1590. doi:10.1128/EC.00150-08
Untergasser, A., Cutcutache, I., Koressaar, T., Ye, J., Faircloth, B. C., Remm, M. and Rozen, S. G. (2012). Primer3–new capabilities and interfaces. *Nucleic Acids Res.* **40**, e115-e115. doi:10.1093/nar/gks596
Vale, R. D. and Fletterick, R. J. (1997). The design plan of kinesin motors. *Annu. Rev. Cell Dev. Biol.* **13**, 745-777. doi:10.1146/annurev.cellbio.13.1.745
van Dam, T. J. P., Townsend, M. J., Turk, M., Schlessinger, A., Sali, A., Field, M. C. and Huynen, M. A. (2013). Evolution of modular intraflagellar transport from a coatomer-like progenitor. *Proc. Natl. Acad. Sci. USA* **110**, 6943-6948. doi:10.1073/pnas.1221011110
Vashishtha, M., Walther, Z. and Hall, J. L. (1996). The kinesin-homologous protein encoded by the Chlamydomonas FLA10 gene is associated with basal bodies and centrioles. *J. Cell Sci.* **109**, 541-549.
Verhey, K. J., Dishinger, J. and Kee, H. L. (2011). Kinesin motors and primary cilia. *Biochem. Soc. Trans.* **39**, 1120-1125. doi:10.1042/BST0391120
Vickerman, K. (1969). On the surface coat and flagellar adhesion in trypanosomes. *J. Cell. Sci.* **5**, 163-193.
Vickerman, K. and Preston, T. M. (1970). Spindle microtubules in the dividing nuclei of trypanosomes. *J. Cell Sci.* **6**, 365-383.
Vukajlovic, M., Dietz, H., Schliwa, M. and Ökten, Z. (2011). How kinesin-2 forms a stalk. *Mol. Biol. Cell* **22**, 4279-4287. doi:10.1091/mbc.e11-02-0112
Wachter, S., Jung, J., Shafiq, S., Basquin, J., Fort, C., Bastin, P. and Lorentzen, E. (2019). Binding of IFT22 to the intraflagellar transport complex is essential for flagellum assembly. *EMBO J.* **38**, e101251. doi:10.15252/embj.2018101251
Wang, Z., Morris, J. C., Drew, M. E. and Englund, P. T. (2000). Inhibition of Trypanosoma brucei gene expression by RNA interference using an integratable vector with opposing T7 promoters. *J. Biol. Chem.* **275**, 40174-40179. doi:10.1074/jbc.M008405200
Wang, M., Gheiratmand, L. and He, C. Y. (2012). An interplay between Centrin2 and Centrin4 on the bi-lobed structure in Trypanosoma brucei. *Mol. Microbiol.* **83**, 1153-1161. doi:10.1111/j.1365-2958.2012.07998.x
Wedaman, K. P., Meyer, D. W., Rashid, D. J., Cole, D. G. and Scholey, J. M. (1996). Sequence and submolecular localization of the 115-kD accessory subunit of the heterotrimeric kinesin-II (KRP85/95) complex. *J. Cell Biol.* **132**, 371-380. doi:10.1083/jcb.132.3.371
Wheeler, R. J., Scheumann, N., Wickstead, B., Gull, K. and Vaughan, S. (2013). Cytokinesis in Trypanosoma brucei differs between bloodstream and tsetse trypomastigote forms: implications for microtubule-based morphogenesis and mutant analysis. *Mol. Microbiol.* **90**, 1339-1355. doi:10.1111/mmi.12436
Wickstead, B. and Gull, K. (2006). A "holistic" kinesin phylogeny reveals new kinesin families and predicts protein functions. *Mol. Biol. Cell* **17**, 1734-1743. doi:10.1091/mbc.e05-11-1090
Wickstead, B., Gull, K. and Richards, T. A. (2010a). Patterns of kinesin evolution reveal a complex ancestral eukaryote with a multifunctional cytoskeleton. *BMC Evol. Biol.* **10**, 110. doi:10.1186/1471-2148-10-110
Wickstead, B., Carrington, J. T., Gluenz, E. and Gull, K. (2010b). The expanded Kinesin-13 repertoire of trypanosomes contains only one mitotic Kinesin indicating multiple extra-nuclear roles. *PLoS ONE* **5**, e15020. doi:10.1371/journal.pone.0015020
Wirtz, E., Leal, S., Ochatt, C. and Cross, G. A. M. (1999). A tightly regulated inducible expression system for conditional gene knock-outs and dominant-negative genetics in Trypanosoma brucei. *Mol. Biochem. Parasitol.* **99**, 89-101. doi:10.1016/S0166-6851(99)00002-X
Woods, A., Sherwin, T., Sasse, R., MacRae, T. H., Baines, A. J. and Gull, K. (1989). Definition of individual components within the cytoskeleton of Trypanosoma brucei by a library of monoclonal antibodies. *J. Cell Sci.* **93**, 491-500.
Yu, Z., Liu, Y. and Li, Z. (2012). Structure-function relationship of the Polo-like kinase in Trypanosoma brucei. *J. Cell Sci.* **125**, 1519-1530. doi:10.1242/jcs.094243

Zhang, X., An, T., Pham, K. T. M., Lun, Z.-R. and Li, Z. (2019). Functional analyses of cytokinesis regulators in bloodstream stage trypanosoma brucei parasites identify functions and regulations specific to the life cycle stage. *mSphere* **4**, e00199-19. doi:10.1128/mSphere.00199-19

Zhou, Q., Hu, H. and Li, Z. (2014). New insights into the molecular mechanisms of mitosis and cytokinesis in trypanosomes. *Int. Rev. Cell Mol. Biol.* **308**, 127-166. doi:10.1016/B978-0-12-800097-7.00004-X

Zhou, Q., Hu, H., He, C. Y. and Li, Z. (2015). Assembly and maintenance of the flagellum attachment zone filament in Trypanosoma brucei. *J. Cell Sci.* **128**, 2361-2372. doi:10.1242/jcs.168377

Zhou, Q., An, T., Pham, K. T. M., Hu, H. and Li, Z. (2018). The CIF1 protein is a master orchestrator of trypanosome cytokinesis that recruits several cytokinesis regulators to the cytokinesis initiation site. *J. Biol. Chem.* **293**, 16177-16192. doi:10.1074/jbc.RA118.004888

S1A
Topology of phylogenetic relationships within kinesin-2 family (incl. 2A -2D subgroups) from kinesin superfamily motor domain phylogenetic inference analysis by Wickstead, *et al.*, 2010.

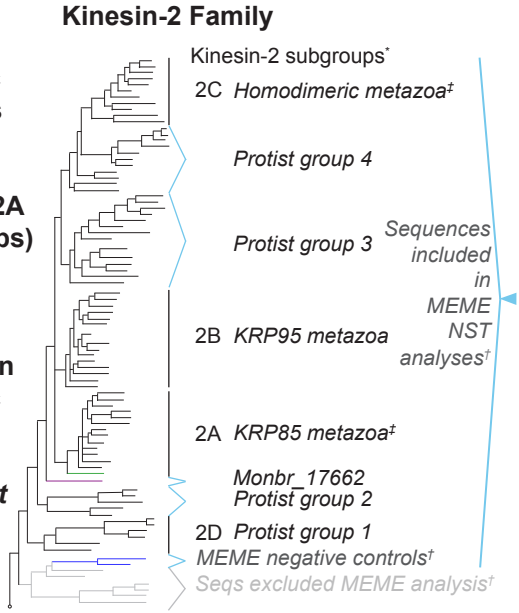

S1B

Significant* NST motifs identified for Meme 83

Mtf m#	Wid (aa)	# Site	E-val**	Motif sequence LOGO
1	31	67	-1185	
2	22	56	-320	
3	31	46	-398	
4	12	54	-151	
5	50	15	-192	
6	16	42	-156	
7	22	40	-98	
8	31	39	-89	
9	16	29	-70	
10	12	29	-63	

S1B *(continued)*

Mtf m#	Wid (aa)	# Site	E-val**	Motif sequence LOGO
11	16	13	-61	
12	22	42	-37	
13	14	10	-22	
14	43	3	-21	
			(Motif not evaluated)	
15	50	3	-18	
16	35	5	-12	
17	15	8	-12	
18	49	3	-11	
19	35	3	-08	
20	50	3	-12	
21	08	10	-07	
22	31	6	-05	
23	12	21	-05	
24	09	13	-04	
25	42	3	-03	
29	44	5	+01	

S1C Schematic of M83 motifs with motif widths to scale + color -coded motif groups (per S2A), ranked by increasing E-value

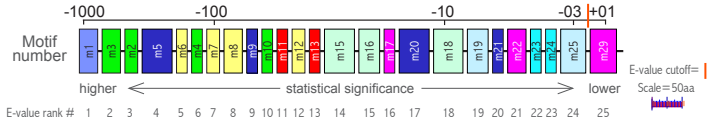

Fig. S1. Kinesin-2 family phylogeny and NST motifs. **(A)** Kinesin-2 family phylogentic tree topology adapted from the previous analysis by using motor domain sequences; branch lengths shown do not indicate evolutionary distances. Symbols: †Our early MEME analyses showed these NST sequences to be distinct from remaining kinesin-2 sequences; for additional information see Table S3A. ‡Monbr_16629 and Monbr_23354 of the holozoan *M. brevicolis* were previously assigned to subgroups 2A and 2C, respectively (Wickstead et al., 2010). Monbr_23354 had a putative NST domain too short for MEME analysis. **(B)** Kinesin-2 motor domain (MD) sequences are more highly conserved than kinesin-2 NST sequences (see Table S1 for MD sequence comparisons, and Table S2 for NST sequence comparisons). Our NST analyses relied primarily upon the MEME tool suite (see main text), which can identify conserved motifs independently of sequence alignment or motif order. We carried out over 80 MEME runs because of variation between runs due to differences in run parameters and sequences used as described in Materials and Methods. In the figure are the 25 statistically significant NST motifs (based on MEME-determined individual motif overall E-values), plus one additional motif identified, from a single representative run (MEME 83). Shown are: motif number (Mft m#); optimal width (amino acids or aa); the total number of significant, non-overlapping, independent motifs identified in the data set (# sites); the E-value overall statistical significance measure for each motif as defined in (expressed as integer (e.g. -10), equivalent to 1 x 10E-value with lower E-values being more statistically significant), with a motif overall E-value significance cutoff of -02 as recommended in MEME, with the exception of motif 29 which had an E-value = 1; and each motif's MEME-identified amino acid consensus sequence (LOGO) as determined (within MEME) using the sequence display program LOGO (Crooks et al., 2004; Schneider and Stephens, 1990). Motif E-values are calculated in MEME based on combined motif p-values on individual sequences, with only significant motif p-values ($\leq 1 \times 10^{-10}$) on individual sequences used to calculate E-values. **(C)** Schematic of individual motifs from S1B arranged from left to right in order of increasing E-values (from most to least significant). Widths of individual motifs are displayed to scale for motifs having 16 aa or greater; motif widths of 8 - 15 aa are displayed as equal to 16 aa for visibility. Each motif is color-coded according to the motif group to which it is assigned. Orange bar indicates E-value = -02 statistical significance cutoff recommended by MEME authors. Scale bar = 50 aa (with the exceptions stated above).

References:

Crooks, G. E., Hon, G., Chandonia, J.-M. and Brenner, S. E. (2004). WebLogo: a sequence logo generator. *Genome Res.* **14,** 1188–1190.

Schneider, T. D. and Stephens, R. M. (1990). Sequence logos: a new way to display consensus sequences. *Nucleic Acids Res.* **18,** 6097–6100.

Wickstead, B., Gull, K. and Richards, T. A. (2010). Patterns of kinesin evolution reveal a complex ancestral eukaryote with a multifunctional cytoskeleton. *BMC Evol. Biol.* **10,** 110.

S2A

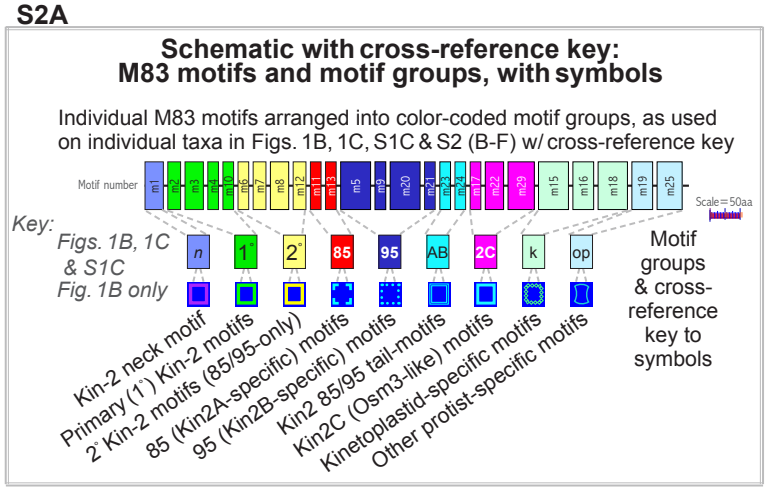

S2B Sequence motifs key: motif heights indicate *p*-value ranges

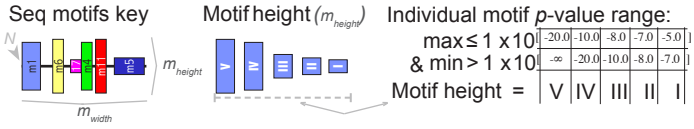

S2C Kin2A, 2B, 2C motifs & motif order are broadly conserved***

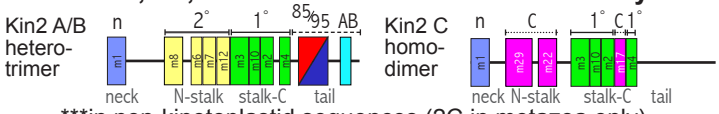

***in non-kinetoplastid sequences (2C in metazoa only)

S2E TbKin2a and select kinetoplastid homologs

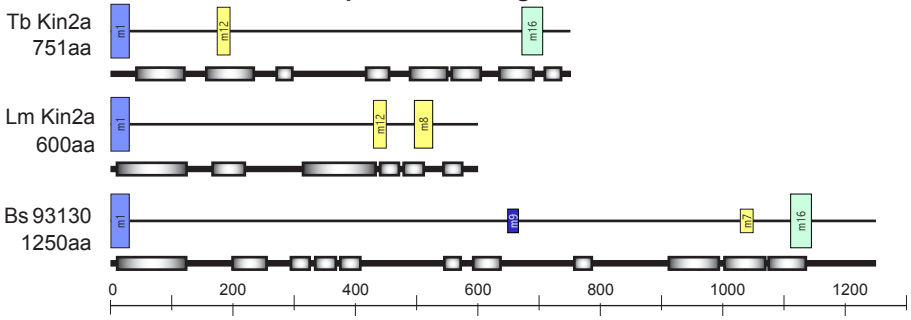

S2F 1 Shared 2C motif on TbKin2b, kinetoplastid homologs & metazoan 2C taxa

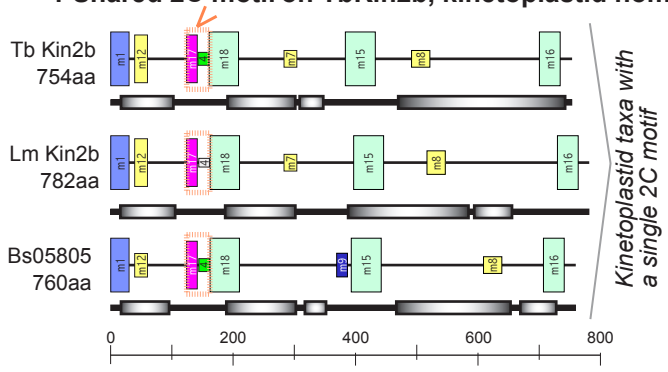

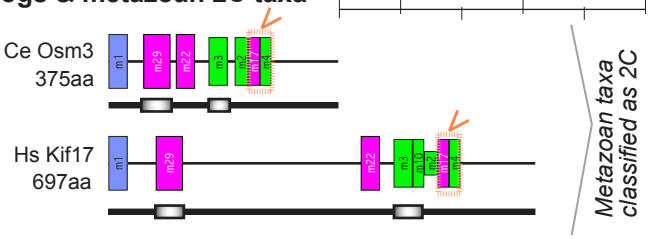

†††Location of 2C (m17) + 1°Kin2 (m4) motifs (metazoa) or 2C (m17) + low p-value/ partial 1°Kin2 (m4) motif (kinetoplastids)

S2D Selected sequences with conserved 1° Kin2 & 2° Kin2 + (85 / 95 motifs)†

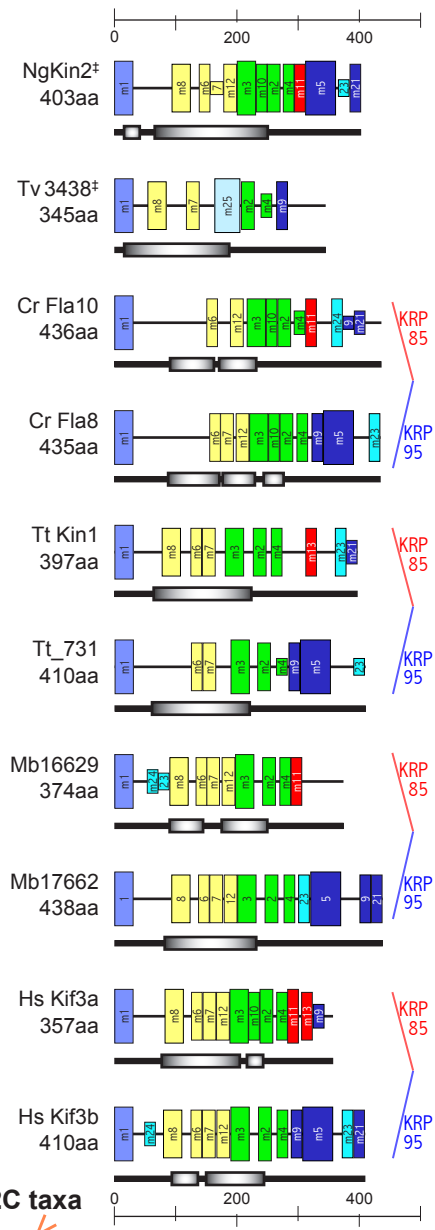

Fig. S2. Kinesin-2 NST motifs and motif groups in individual sequences. **(A)** Schematic of individual motifs arranged into motif groups. Motif groups are cross-referenced to motif group symbols that are used in Fig. 1 (B-D). In Fig. 1 and Fig. S2, references to motif group 2A/ KRP85/ 85 are equivalent, as are references to motif group 2B/ KRP95/ 95, and motif group 2C/ OSM3. See Fig. S1C legend for motif width scaling information. **(B)** Key showing how the height of motif boxes on individual sequence scales with motif p-value ranges. Roman numerals V to I show sequence-specific individual motif p-value ranges as follows: V = p-value $\leq 1 \times 10^{-20}$, IV = p-value $>1 \times 10^{-20}$ and $\leq 1 \times 10^{-10}$, III = p-value $>1 \times 10^{-10}$ and $\leq 1 \times 10^{-08}$, II = p-value $>1 \times 10^{-08}$ and $\leq 1 \times 10^{-07}$, I = p-value $>1 \times 10^{-07}$ and $\leq 1 \times 10^{-05}$. **(C)** Schematic showing that motif order is generally conserved among kinesin-2 proteins as depicted. **(D)** NST motifs for a selected group of heterotrimeric kinesin-2A and -2B proteins across a broad evolutionary backdrop illustrate sequence motif conservation noted in (C). In particular, we observed a high frequency of 1° motifs 2, 3, 4 on taxa, especially signature residues [F - I - P] that terminate 1° motif 2, and [W/Y - 6X (with 1-3 E/D) - W] in 1° motif 4, which were observed previously in *Xenopus laevis* (De Marco et al., 2001). **(E)** NST motifs for TbKin2a and homologs LmKin2a and Bs93130. One common kinesin-2 motif (2° motif 12) had a significant p-value on 2 of 3 taxa. **(F)** NST motifs for TbKin2b, the related LmKin2b and Bs05805, as well as the kinesin-2C proteins CeOSM3 and HsKif17. Note that 2C motif 17 is followed directly by 1° motif 4 for both metazoan taxa, 1° motif 4 for *T. brucei* and *B. saltans* sequences and a possible (low p-value) amino acid signature for *L. major* (not shown). TbKin2b and kinetoplastid homologs also have a predicted 2° motif 12, here located consistently just after neck domain of the 3 kinetoplastid proteins.

References:

De Marco, V., Burkhard, P., Le Bot, N., Vernos, I. and Hoenger, A. (2001) Analysis of heterodimer formation by Xklp3A/B, a newly cloned kinesin-II from *Xenopus laevis*. *EMBO J* **20**, 3370–3379.

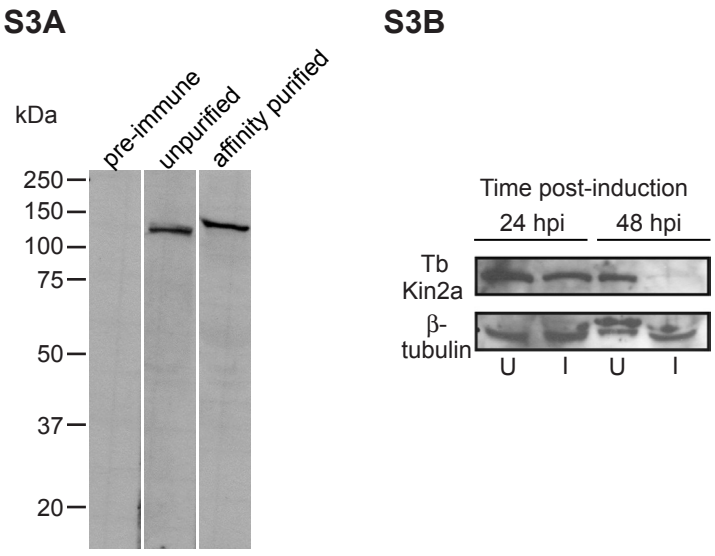

Fig. S3. (A) Western blots of whole-cell extracts from T. brucei probed with pre-immune rabbit serum (left), unpurified post-immune rabbit serum (center), and affinity-purified anti-TbKin2a IgG rabbit polyclonal antibody (right). Predicted molecular weight of full-length TbKin2a (1088 aa) protein = 122.72 kDa. **(B)** Western blots of whole-cell extracts probed with rabbit anti-TbKin2a IgG primary antibody (top), and mouse anti-β-tubulin IgG (KMX) primary antibody (bottom), each followed by applicable secondary anti-IgG antibody conjugated to horseradish peroxidase, from TbKin2a RNAi uninduced (U) and induced (I) cells at 24 and 48 hours post induction (hpi). Note TbKin2a protein levels remain significant at 24 hpi, and are reduced but visible at 48 hpi, indicating residual TbKin2a activity may persist until relatively late during RNAi induction period. See Figure 5A for control (wild-type) cell immunoblots.

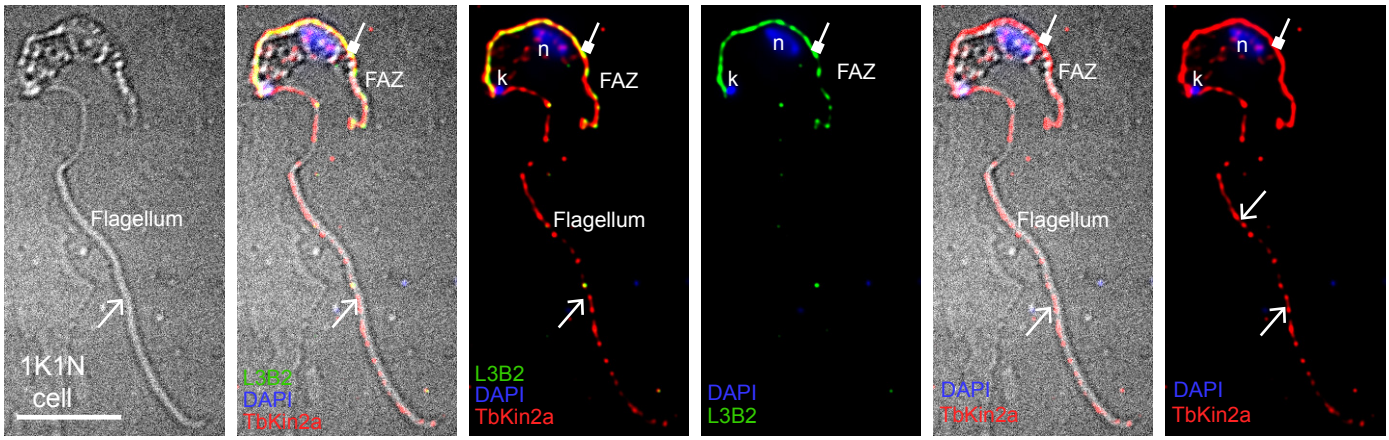

Fig. S4. DIC and immunofluorescence images of cells grown in media with 20 mM citrate and 5 mM $MgCl_2$ for ~30 h to chelate Ca^{2+} and induce flagellar detachment. Cells were stained for TbKin2a (red), FAZ protein TbFAZ1 (green, L3B2) and DNA (blue, DAPI). Immunoflourescence images are 2D maximum intensity projections from 3D deconvolved z-stacks. Symbols are the same as used in Fig. 4. Bar = 7.4 µm

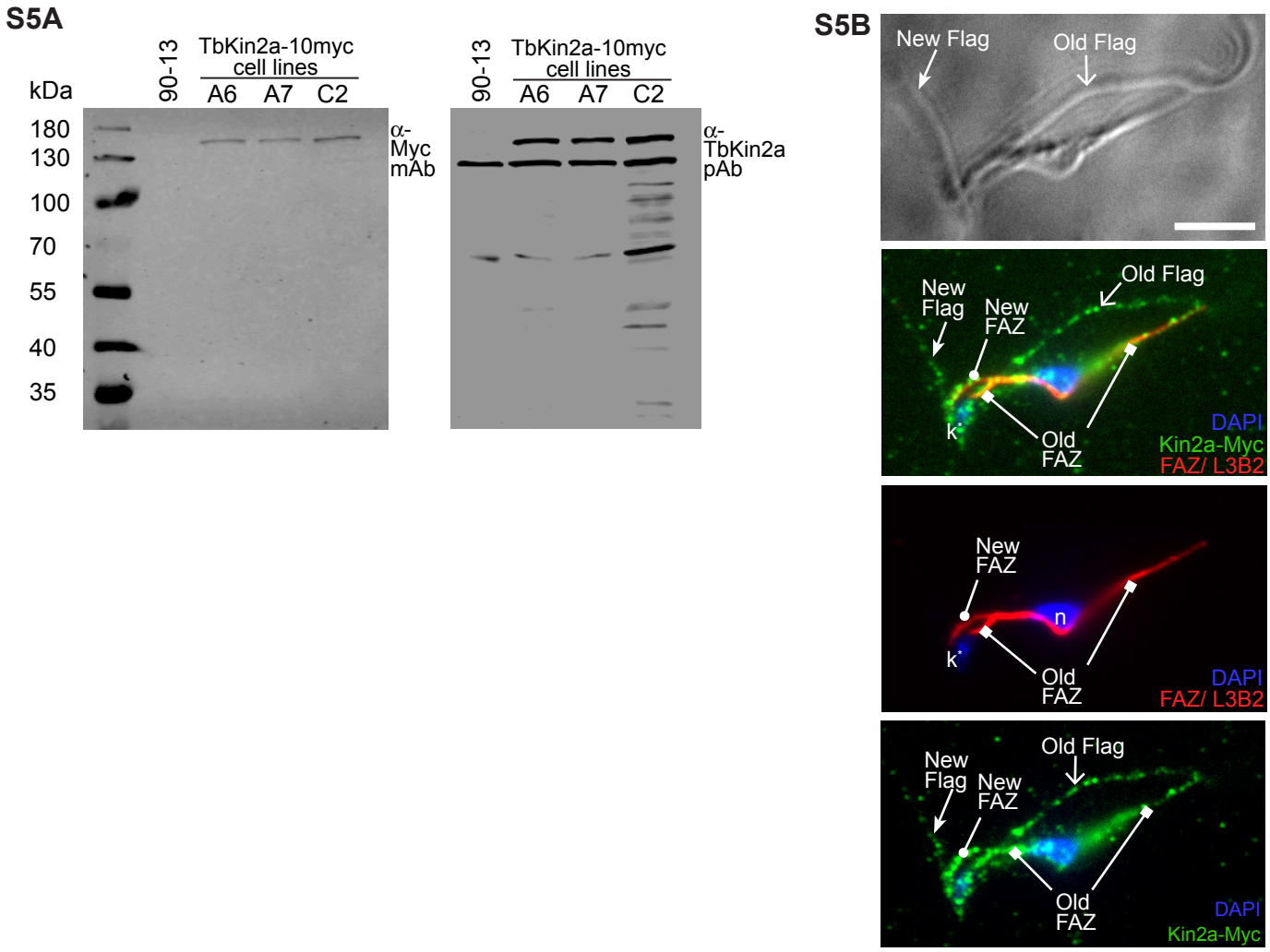

Fig. S5. (A) Western blots showing endogenous expression of full length TbKin2a with a C-terminal Myc fusion tag (TbKin2a-Myc) in three *T. brucei* BSF clonal cell lines (A6, A7, C2) transfected with pPOTv7, and 90-13 negative control, probed with anti-Myc mouse IgG1 monoclonal antibody 9E10 (left) and anti-TbKin2a rabbit polyclonal antibody (right). **(B)** DIC and immunofluorescence images of a detergent extracted *T. brucei* BSF clone-A7 cell, methanol-fixed and stained for TbKin2a-Myc with anti-Myc mouse IgG2a monoclonal antibody 9B11 (catalog #2276, Cell Signaling Technology, Danvers, MA) (red), FAZ protein TbFAZ1 with anti-TbFAZ mouse IgG1 monoclonal antibody L3B2 (green), and DNA with DAPI fluourescent dye (blue). Secondary goat anti-mouse monoclonal antibodies conjugated to AlexaFluor red and green fluorescent dyes were, respectively, mouse IgG2a and IgG1 isotype-specific. Bar = 5 µm.

Table S1. Kinesin-2 Motor Domain Sequences Identity Matrix

Click here to Download Table S1

Table S2. Kinesin-2 NST Domain Sequences Identity Matrix

Click here to Download Table S2

Table S3. Kinesin-2 sequence information and reconciliation, parts 3A and 3B

Click here to Download Table S3A3B

Table S4. Taxa NST FASTA File Names and Sequences

Click here to Download Table S4

Table S5. Primer Sequences Used

Click here to Download Table S5